



# The relative importance of macrophysical and cloud albedo changes for aerosol-induced radiative effects in closed-cell stratocumulus: insight from the modelling of a case study

Daniel P. Grosvenor<sup>1</sup>, Paul R. Field<sup>1,2</sup>, Adrian A. Hill<sup>2</sup>, and Benjamin J. Shipway<sup>2</sup>

<sup>1</sup>School of Earth and Environment, University of Leeds, Leeds, LS2 9JT, UK

<sup>2</sup>Met Office, Exeter, UK

Correspondence to: Daniel P. Grosvenor (daniel.p.grosvenor@gmail.com)

Received: 14 November 2016 – Discussion started: 23 November 2016

Revised: 2 March 2017 – Accepted: 15 March 2017 – Published: 20 April 2017

**Abstract.** Aerosol–cloud interactions are explored using 1 km simulations of a case study of predominantly closed-cell SE Pacific stratocumulus clouds. The simulations include realistic meteorology along with newly implemented cloud microphysics and sub-grid cloud schemes. The model was critically assessed against observations of liquid water path (LWP), broadband fluxes, cloud fraction ( $f_c$ ), droplet number concentrations ( $N_d$ ), thermodynamic profiles, and radar reflectivities.

Aerosol loading sensitivity tests showed that at low aerosol loadings, changes to aerosol affected shortwave fluxes equally through changes to cloud macrophysical characteristics (LWP,  $f_c$ ) and cloud albedo changes due solely to  $N_d$  changes. However, at high aerosol loadings, only the  $N_d$  albedo change was important. Evidence was also provided to show that a treatment of sub-grid clouds is as important as order of magnitude changes in aerosol loading for the accurate simulation of stratocumulus at this grid resolution.

Overall, the control model demonstrated a credible ability to reproduce observations, suggesting that many of the important physical processes for accurately simulating these clouds are represented within the model and giving some confidence in the predictions of the model concerning stratocumulus and the impact of aerosol. For example, the control run was able to reproduce the shape and magnitude of the observed diurnal cycle of domain mean LWP to within  $\sim 10 \text{ g m}^{-2}$  for the nighttime, but with an overestimate for the daytime of up to  $30 \text{ g m}^{-2}$ . The latter was attributed to the uniform aerosol fields imposed on the model, which meant

that the model failed to include the low- $N_d$  mode that was observed further offshore, preventing the LWP removal through precipitation that likely occurred in reality. The boundary layer was too low by around 260 m, which was attributed to the driving global model analysis. The shapes and sizes of the observed bands of clouds and open-cell-like regions of low areal cloud cover were qualitatively captured. The daytime  $f_c$  frequency distribution was reproduced to within  $\Delta f_c = 0.04$  for  $f_c > \sim 0.7$  as was the domain mean nighttime  $f_c$  (at a single time) to within  $\Delta f_c = 0.02$ . Frequency distributions of shortwave top-of-the-atmosphere (TOA) fluxes from the satellite were well represented by the model, with only a slight underestimate of the mean by 15%; this was attributed to near-shore aerosol concentrations that were too low for the particular times of the satellite overpasses. TOA long-wave flux distributions were close to those from the satellite with agreement of the mean value to within 0.4%. From comparisons of  $N_d$  distributions to those from the satellite, it was found that the  $N_d$  mode from the model agreed with the higher of the two observed modes to within  $\sim 15\%$ .

---

*Copyright statement.* The works published in this journal are distributed under the Creative Commons Attribution 3.0 License. This licence does not affect the Crown copyright work, which is reusable under the Open Government Licence (OGL). The Creative Commons Attribution 3.0 License and the OGL are interoperable and do not conflict with, reduce, or limit each other.

© Crown copyright 2017

## 1 Introduction

In this paper we describe 1 km horizontal grid-spacing simulations of marine stratocumulus clouds nested within a global operational analysis framework that provides realistic meteorological initial conditions and lateral boundary forcing. A grid spacing of this order bridges the gap between large eddy simulation (LES) and global model resolution, allowing larger domains than possible with LES, but the direct representation of more detailed processes than is possible with global models. We perform the first tests for stratocumulus of a newly implemented microphysics package that includes a detailed representation of the effects of aerosol upon clouds and a diagnostic cloud scheme. We use this model to examine the response of the cloud field to varying aerosol concentrations.

Stratocumulus clouds are the dominant cloud type in terms of area, covering over one-fifth of the Earth's surface in the annual mean (Wood, 2012). They exert a strong net negative radiative effect that has a major impact on Earth's radiative balance (Hartmann et al., 1992) and only a small change in their properties would have a large radiative impact (e.g. Latham et al., 2008). The albedo and the spatial coverage of stratocumulus clouds are affected by both their macrophysical and microphysical properties, with aerosol potentially playing a key role in modulating both of these aspects. If this is the case, then the accurate representation of cloud–aerosol interactions would be needed in order to make robust predictions about the response of stratocumulus to climate change and anthropogenic aerosol changes. Furthermore, since uncertainties in the representation of stratocumulus have been identified as one of the major sources of uncertainty in climate model predictions (Bony, 2005; Soden and Vecchi, 2011), it follows that the treatment of aerosol will influence this uncertainty if the aerosol has a significant cloud impact.

Stratocumulus clouds are also important for numerical weather prediction (NWP) because they modulate the surface temperature through its influence on downwelling shortwave and long-wave radiation at the surface. Furthermore, their influence on visibility is a major consideration for aircraft operations. There is therefore a strong impact on both commercial and general public weather forecasts and applications.

For the climate system, the radiative impact of stratocumulus is strongly dependent on macrophysical properties such as cloud fraction or cloud liquid water path (LWP), which are likely to be heavily influenced by large-scale circulation and meteorological factors. However, microphysical processes can also influence the macrophysical cloud properties, as well as having important radiative impacts in their own right. If all else is equal, i.e. a fixed liquid water content (LWC), increasing the concentration of cloud condensation nuclei (CCN) leads to smaller droplets that in turn produce more reflective clouds (Twomey, 1977). The reduction of droplet sizes is also associated with the suppression

of precipitation. Since this removes the main sink for water in a cloud, it was suggested that precipitation suppression via increases in aerosol would increase LWP and cloud lifetime (e.g. Albrecht, 1989), an idea that has been backed up by LES modelling studies (Berner et al., 2013; Feingold et al., 2015; Ackerman et al., 2004, hereafter A04). However, A04 showed that this is only true for precipitating clouds; once precipitation had been suppressed, further aerosol increases led to cloud thinning (LWP decrease) via increases in entrainment. Mechanisms for this effect are discussed in Bretherton et al. (2007) and Hill et al. (2009). Observation studies have also demonstrated a lack of LWP increase in marine stratocumulus at high aerosol concentrations (e.g. Ackerman et al., 2000; Platnick et al., 2000; Coakley and Walsh, 2002).

Changes in precipitation and LWP that result from changes in aerosol can also be accompanied by changes in cloud fraction (Stevens et al., 1998; Berner et al., 2013, hereafter B13). An example of this is the occurrence of pockets of open cells (POCs). POCs constitute regions of open cells with low cloud fraction in amongst high-cloud-fraction closed-cell regions (Wood et al., 2011a). It has been suggested that the enhancement of precipitation by reduced aerosol concentrations can cause a transition between a state of closed and open cells within stratocumulus (Rosenfeld et al., 2006), which is then enhanced by a positive feedback mechanism that has been called the “runaway precipitation sink” (Feingold and Kreidenweis, 2002), whereby precipitation leads to a reduction in the available CCN. All else being equal, reducing CCN leads to larger drops that enhance the formation of precipitation, promoting the removal of more CCN. High-resolution idealised LES modelling supports this idea (B13) and shows that these processes occur at smaller spatial scales than can be captured explicitly by general circulation models (GCMs).

A compromise between LES and GCMs is a coarser-resolution ( $\sim 1$  km) regional model that can simulate larger domains for the same or less computational cost as an LES. Regional models have the advantage over LES in that they are driven by meteorological analyses that can capture the relevant large-scale dynamic and thermodynamic structure, allowing results to be more easily compared to real observations. Aerosol effects can also be considered relative to dynamical forcing or meteorology effects. However, we also note that many models have the ability to nest down from regional model resolution to LES resolution (including the one used in this study), although the computational cost for high-resolution nests can be prohibitive for large domains. Techniques for the better coupling of (non-LES) atmospheric models to high-resolution LES nests (with non-periodic boundary conditions) now exist and have been shown to compare well to observations (e.g. Chow et al., 2006; Xue et al., 2014, 2016).

It is an open question whether kilometre-scale grid spacings are adequate to simulate the important processes in-

volved in marine stratocumulus. For example, Boutle and Abel (2012, hereafter BA12) showed that a mesoscale model with a 1 km grid spacing could capture closed-cell stratocumulus well, but they did not look at open-cell behaviour. Results from WRF-Chem at coarser grid spacings (9 km, Yang et al., 2011; 12 km, Saide et al., 2012; 14 km, George et al., 2013), where the representation of stratocumulus is reliant on boundary layer parameterizations, have also shown reasonable agreement with observations. Whilst the coarser-resolution models may capture the general features of closed-cell stratocumulus, the simulation of open cells is likely to be more difficult owing to the smaller size of the precipitating and updraft regions and the small scales over which aerosol–cloud interactions occur. It is unclear whether the combination of boundary layer parameterizations and microphysics schemes used in the coarser models will encapsulate the correct response to aerosols.

In this paper we present results using a regional nested configuration of the Met Office Unified Model (UM). It is driven by realistic meteorology and includes a new microphysics scheme called CASIM (Cloud AeroSol Interaction Microphysics; see Sect. 2.1.2 for details) designed to simulate the processes important to aerosol–cloud interactions. Simulating a well-observed case allows the critical assessment of the model against a wide range of relevant observations. By demonstrating that the model is capable of reproducing the observations, we can argue that the model captures the important physics and will provide a reliable baseline for predicting the influence of aerosol on this stratocumulus cloud system.

Thus, we aim to address the following questions:

1. Can a regional model produce a realistic representation of stratocumulus clouds when compared to a diverse range of observations?
2. How do the modelled clouds respond to aerosol?
3. What is the relative importance of macrophysical and cloud albedo changes for aerosol-induced radiative effects?
4. What is the relative importance of the sub-grid cloud scheme?

## 2 Data and methods

For this case study we simulate a near-coastal region of the SE Pacific (see Fig. 1) for the period 12–14 November 2008, during which time mostly closed-cell stratocumulus clouds were observed. This period coincides with the VOCALS field campaign, which took place in this region and provided a variety of cloud, aerosol, and meteorological measurements made from airborne, ship, radiosonde, and buoy observational platforms (Wood et al., 2011b). A variety of satellite

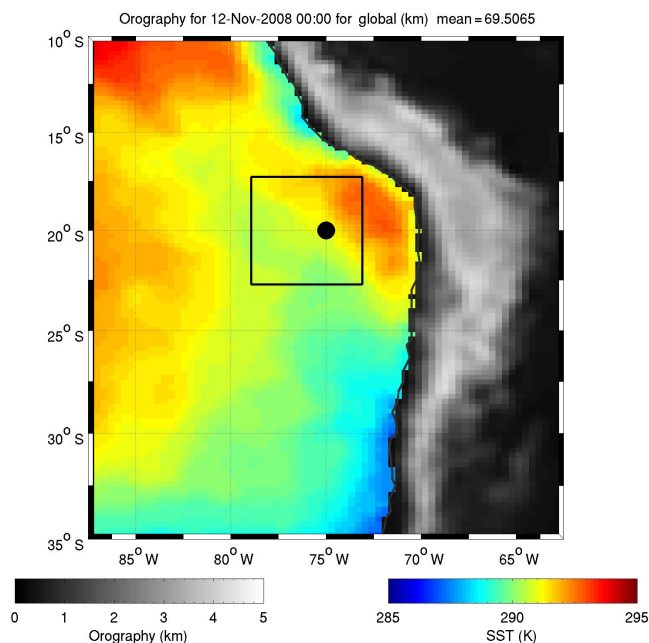


**Figure 1.** A map of the SE Pacific region with the 1 km model domain shown as a black box. The colours show the orography over land and the sea-surface temperature over the ocean, both at the resolution of the global model (N512;  $\sim 39 \text{ km} \times 26 \text{ km}$  resolution at the Equator for  $dx \times dy$ ). The black dot shows the location of the RV *Ronald H. Brown* ( $20^\circ \text{ S}$ ,  $75^\circ \text{ W}$ ).

data are also available. Further details of the simulations and the observations used are now described.

### 2.1 Model details

In this study we use the NWP configuration of the UK Met Office UM. The global model used here is the GA6 configuration of the UM at N512 resolution ( $\sim 39 \text{ km} \times 26 \text{ km}$  resolution at the Equator for  $dx \times dy$ ) with 70 vertical levels below 80 km that are quadratically spaced, giving more levels near the surface. This is run in forecast mode for 2 days (12–14 November) based on an initial field from the UM global operational analysis. The global run provides the initial conditions and forces the lateral boundaries for the wind, moisture, temperature, and condensed water fields for a single 1 km resolution nest centred at  $20^\circ \text{ S}$ ,  $76^\circ \text{ W}$  of  $600 \times 600 \text{ km}$  size (Fig. 1). This places the domain near the coast, but ensures that it covers only oceanic grid-points, which reduces the dynamical and computational complexity. The domain sits in the heart of the region where the VOCALS field campaign aircraft measurements took place (mostly in a transect along  $20^\circ \text{ S}$  between the coast and  $90^\circ \text{ W}$ ) and means that the location of the RV *Ronald H. Brown* during the period ( $20^\circ \text{ S}$ ,  $75^\circ \text{ W}$ ) is near the centre of the domain (see Fig. 1 for the location of the ship). The region consists of very high and steep orography on the coast, with the model predicting warm sea-surface temperatures

**Table 1.** The model vertical grid spacing ( $dz$ ) of the inner 1 km nest as a function of height ( $z$ ) for the boundary layer.

Model level	$z$ (m)	$dz$ (m)
1	2.50	2.50
2	13.33	10.83
3	33.33	20.00
4	60.00	26.67
5	93.33	33.33
6	133.33	40.00
7	180.00	46.67
8	233.33	53.33
9	293.33	60.00
10	360.00	66.67
11	433.33	73.33
12	513.33	80.00
13	600.00	86.67
14	693.33	93.33
15	793.33	100.00
16	900.00	106.67
17	1013.33	113.33
18	1133.33	120.00
19	1260.00	126.67
20	1393.33	133.33
21	1533.33	140.00

(SSTs) just offshore of the coast at the latitudes of the model domain, which reduce with distance offshore until just west of 80° W when they start to increase again.

The 1 km inner nest also employs 70 vertical levels, but with a lower domain top of 40 km and thus a higher vertical resolution. Table 1 shows that the vertical resolution near the top of the boundary layer for the inner nest ( $\sim 1$ – $1.5$  km) is around 100–140 m. The 1 km nest uses a rotated pole coordinate system whose equator is situated at the centre of the domain. A parametrized convection scheme is not required at high resolution since the model is likely to be convection permitting.

The global simulation uses the operational microphysics scheme based on Wilson and Ballard (1999), which is a single moment scheme in that it does not represent the number concentrations of hydrometeors. For the 1 km nest runs we primarily use the newly implemented double-moment CASIM aerosol scheme that is described in Sect. 2.1.2.

### 2.1.1 A sub-grid cloud scheme

The recent previous studies of stratocumulus with the UM that employed high-resolution nests, e.g. BA12, used a sub-grid cloud scheme (Smith, 1990) that was linked to the Wilson and Ballard (1999) microphysics scheme. The sub-grid cloud scheme parameterizes the variability in relative humidity (RH) that occurs in reality within a grid box, which may allow cloud to form even if the mean grid-box RH is below 100 %. This can be important for stratocumulus since

the presence of some liquid cloud water generates long-wave cooling at cloud top, which creates instability within the boundary layer. This drives turbulent overturning that can in turn create more cloud (i.e. a positive feedback).

When CASIM was implemented into the UM, it was done so with no sub-grid cloud scheme. In this configuration there was a large under-prediction in the amount of stratocumulus (see Sect. 3.2.2). Therefore, work was undertaken to implement and adapt the Smith (1990) approach to allow it to work with a multi-moment bulk scheme such as CASIM. Details of this implementation are provided in Appendix A.

### 2.1.2 The CASIM microphysics scheme

CASIM is a new multi-moment microphysics scheme for the UM that includes the effects of aerosol upon clouds and vice versa. This provides enhanced capability over the old operational scheme in which the cloud droplet concentration was constant throughout the domain.

As with other bulk microphysics schemes, the cloud and rainwater are separated into two hydrometeor classes. In each class the drop size distributions are described using a gamma distribution with a prescribed shape parameter and prognosed bulk mass and number concentration, i.e. double moment cloud and rain (for details on the multi-moment implementation, see Shipway and Hill, 2012). In this study, ice microphysics is not switched on since only warm clouds were present in the study area.

If a model grid box is deemed to be sufficiently humid by the above-mentioned cloud scheme, then cloud water condenses and the number of droplets activated is determined using the scheme described in Abdul-Razzak and Ghan (2000), which makes use of explicitly resolved vertical velocity, humidity, and aerosol properties to compute the number concentration of droplets activated. Autoconversion of cloud droplets to rain and droplet accretion is based upon Khairoutdinov and Kogan (2000), and the self-collection of rain follows Beheng (1994). Details on the testing of the warm rain microphysics parameterizations used in CASIM in an idealized framework can be found in Hill et al. (2015). The scheme includes an option for the sedimentation of cloud water; however, this is switched off for most of the runs in this paper. We discuss the effect of switching this on for some test runs in Sect. 4.2. The hydrometeor fall–speed relationship follows Shipway and Hill (2012). Table 2 summarizes the microphysical parameterizations used and Table 3 gives the constants used.

Five different size modes are available to represent soluble and insoluble aerosol, but only a single soluble accumulation mode is used here. The aerosol mode has a lognormal size distribution with a fixed width. In this paper the aerosol is initially spatially uniform in both the vertical and horizontal and the same aerosol profiles are applied as lateral boundary conditions to the inner nest. There are no local sources of aerosol at present. However, aerosol is advected and thus

**Table 2.** CASIM microphysics scheme parameterization summary.

Parameterization	Reference
Aerosol activation	Abdul-Razzak and Ghan (2000)
Autoconversion of droplets to rain	Khairoutdinov and Kogan (2000)
Accretion of droplets by rain	Khairoutdinov and Kogan (2000)
Rain self-collection	Beheng (1994)

concentrations can change locally due to convergence and divergence. Details of the aerosol concentrations used in the different runs of this work are given in the next section. CASIM includes the option of aerosol processing, which includes activation scavenging; in-cloud mechanical processing into fewer, but larger aerosol particles (via collision coalescence); precipitation washout of both in-cloud and out-of-cloud aerosol; and evaporative regeneration. These processes can lead to an overall reduction in the aerosol available for forming cloud droplets. However, aerosol processing is not switched on for the runs in this work, but will be considered in a later paper.

### 2.1.3 Details on model runs and sensitivities

We have performed several model runs that are listed in Table 4. The run denoted as Old-mphys uses the old microphysics scheme (Wilson and Ballard, 1999), which also uses the Smith (1990) sub-grid cloud scheme and has a fixed cloud droplet concentration of  $100 \text{ cm}^{-3}$ . All of the other simulations use the CASIM microphysics. CASIM-Ndvar is the control aerosol case, where the accumulation soluble-mode aerosol has been chosen (the mass mixing ratio was set to  $4.6 \times 10^{-8} \text{ kg kg}^{-1}$ , the number concentration to  $3.8 \times 10^9 \text{ kg}^{-1}$ ) to produce droplet concentrations that are in approximate agreement with those observed (see Sect. 3.2.1). CASIM-Ndvar-RHcrit0.999 is the same as the control run except that the sub-grid cloud scheme has been switched off in order to investigate its impact.

Aerosol sensitivity runs have been performed where the soluble accumulation mode aerosol mass and number have been reduced by factors of 10 and 40 (CASIM-Ndvar-0.1 and CASIM-Ndvar-0.025 respectively) and increased by a factor of 10 (CASIM-Ndvar-10). This range of aerosol concentrations creates clouds with droplet numbers that bracket the range observed during the VOCALS field campaign, as we will show in Sect. 3.2.1.

## 2.2 Observations

Data from a variety of instruments onboard several observational platforms, including satellite, ship, and aircraft, have been used to validate the model. The data used (including error estimates from the literature) are described in Appendix B and summarized in Table 5.

**Table 3.** The microphysical parameters used in the simulations for the equations described in Shipway and Hill (2012).  $\rho_w$  is the density of water.

	Cloud	Rain
Moment description parameters		
$p_1$	0	0
$p_2$	3	3
Size spectra parameters		
$\mu$	0	2.5
Mass–diameter parameters		
$c_x$	$\pi \rho_w/6$	$\pi \rho_w/6$
$d_x$	3	3
Fall–speed parameters		
$a_x$	$3 \times 10^7$	130
$b_x$	2	0.5
$f_x$	0	0
$g_x$	0.5	0.5

## 2.3 Cloud fraction definition

In this paper we choose to define cloud using an LWP threshold of  $20 \text{ g m}^{-2}$ . The use of LWP makes comparisons between model and satellite instruments simpler. A threshold value of  $20 \text{ g m}^{-2}$  represents a conservative estimate of the lower limit of the microwave instruments used to observe LWP.

## 3 Results

### 3.1 General case study features from the observations

Figure 2 shows snapshot satellite images from 13 November, including daytime maps of LWP and  $N_d$  from GOES-10 and a nighttime LWP map from AMSR-E. Both LWP images reveal extensive cloud cover, although it is evident that there are more cloud-free regions in the daytime image. The LWP is much larger at night compared to the daytime (note the different colour bars), which is a well-known feature of the diurnal cycle of stratocumulus and is due to the lack of shortwave heating of cloud tops at night (Wood, 2012). Both the daytime and nighttime plots show that the highest LWP region lies in a NW-to-SE-oriented diagonal band across the region, with thin cloud present both near the coast and much further offshore to the southwest. The model domain (indicated by the blue box) contains both the coastal thin cloud region and the higher LWP values offshore. The high-resolution daytime GOES-10 image shows several cloud-free regions within the general area of the diagonal band (e.g. centred at  $16^\circ \text{ S}, 88^\circ \text{ W}$ ;  $19^\circ \text{ S}, 81^\circ \text{ W}$ ; and  $22^\circ \text{ S}, 77^\circ \text{ W}$ ), which do not

**Table 4.** UM model runs. “Standard  $\text{RH}_{\text{crit}}$ ” refers to the standard profile (listed in Table A1) of the  $\text{RH}_{\text{crit}}$  parameter that is used within the sub-grid cloud parameterization (see Appendix A).

Model label	Description
Old-mphys	Old (3-D) microphysics, with standard $\text{RH}_{\text{crit}}$
CASIM-Ndvar (CONTROL)	CASIM microphysics, variable $N_{\text{d}}$ , standard $\text{RH}_{\text{crit}}$
CASIM-Ndvar-0.025	CASIM-Ndvar with aerosol $\times 0.025$
CASIM-Ndvar-0.1	CASIM-Ndvar with aerosol $\times 0.1$
CASIM-Ndvar-10	CASIM-Ndvar with aerosol $\times 10$
CASIM-Ndvar-RHcrit0.999	CASIM-Ndvar with cloud scheme OFF

appear to be present at night. These regions could be considered as POCs (pockets of open cells) since they constitute large regions of low-cloud-fraction open cells in amongst a region of otherwise closed-cell stratocumulus.

The  $N_{\text{d}}$  map shows the presence of a large spatial gradient with high  $N_{\text{d}}$  values near the coast and low  $N_{\text{d}}$  values offshore, which seem somewhat anticorrelated with LWP. This may indicate correlations caused by meteorology (e.g. two separate air masses), or it could be the result of aerosol feedbacks upon LWP (or a combination of the two). This boundary crosses the UM model domain, splitting it roughly into two halves in terms of LWP, with a low-LWP and high- $N_{\text{d}}$  region to the NE and a high-LWP and low- $N_{\text{d}}$  region in the southwest.

### 3.2 Model validation and aerosol sensitivity

#### 3.2.1 Droplet concentration distributions

Figure 3 shows probability density functions (PDFs) of the cloud droplet number concentration for a snapshot daytime period (14:00 LST on 13 November) for the inner nest of the model domain for both the model and GOES-10 satellite instrument. Since the satellite provides a 2-D field of  $N_{\text{d}}$ , it is necessary to make a 2-D field from the 3-D model data. This is done by taking  $N_{\text{d}}$  at the height of the maximum LWC for each model profile since this helps to avoid the  $N_{\text{d}}$  from spuriously small LWC grid boxes from being included. For similar reasons, data points from both the model and the satellite are ignored if the LWP is less than  $5 \text{ g m}^{-2}$ , but only after the model  $N_{\text{d}}$  and LWP data have been coarse-grained from their native 1 km resolution to that of GOES-10 (4 km).

The observations from GOES-10 show that there is a two-mode PDF, with a mode of very low  $N_{\text{d}}$  ( $\sim 25 \text{ cm}^{-3}$ ) and one at  $215 \text{ cm}^{-3}$ . This reflects the two different air masses that seem to be present, as discussed earlier (Fig. 2, i.e. a near-coastal air mass with high  $N_{\text{d}}$  and an offshore air mass with low  $N_{\text{d}}$ ). The models only capture one of these modes of  $N_{\text{d}}$  since a spatially uniform aerosol field was applied. However, it is conceivable that the low- $N_{\text{d}}$  mode may also be the result of aerosol removal within the precipitating open-cell regions of the stratocumulus since this too can lead to very low  $N_{\text{d}}$  values (B13). Since aerosol processing

and scavenging is not switched on for these runs, the model will not capture the latter process. Using fixed aerosol concentrations allows the exploration of the extreme high- and low-aerosol-loading scenarios without the complications of aerosol source functions and processing. This extra complexity will be explored in a later paper.

The control model (CASIM-Ndvar) has a  $N_{\text{d}}$  distribution that has a similar width (to within  $\sim 15\%$ ) to that of the higher- $N_{\text{d}}$  mode observed by GOES-10, although it has a higher frequency of the higher  $N_{\text{d}}$  values (above  $275 \text{ cm}^{-3}$ ). Despite this, the modal value is lower for the model ( $155 \text{ cm}^{-3}$ ) than for the large mode of GOES-10 ( $215 \text{ cm}^{-3}$ ), although the broadness of the model distribution means that it still has large frequencies of data at the position of the GOES-10 modal value. Given the lack of sensitivity of the modelled clouds to increasing the aerosol by a factor of 10, it seems unlikely that the small differences between the modelled and observed large- $N_{\text{d}}$  mode would have a very large impact on cloud properties. The lack of a lower- $N_{\text{d}}$  mode in the model could be more important. This is explored through the sensitivity tests where we reduce the aerosol.

Figure 3 demonstrates that reducing the aerosol by factors of 10 and 40 (CASIM-Ndvar-0.1 and CASIM-Ndvar-0.025) decreases the mode values of  $N_{\text{d}}$  to 25 and  $3.5 \text{ cm}^{-3}$  respectively. The CASIM-Ndvar-0.025 case produces droplet concentrations that are very low, with no values above  $10 \text{ cm}^{-3}$ . This is consistent with the observations of ultra-clean regions that have been observed in the outflow regions of POCs (Wood et al., 2011a) and so can be considered as a lower realistic bound for aerosol concentrations. The CASIM-Ndvar-10 case produces droplet concentrations of up to around  $3000 \text{ cm}^{-3}$ , although with a 95th percentile of  $1585 \text{ cm}^{-3}$ . Aircraft observations from the VOCALS field campaign reported maximum  $N_{\text{d}}$  values of around  $400 \text{ cm}^{-3}$  in the vicinity of the coast at  $20^\circ \text{ S}$  (Zheng et al., 2011) over the whole campaign period; thus, the modelled  $N_{\text{d}}$  values in the CASIM-Ndvar-10 case are somewhat higher than those likely to occur in reality for this region. However,  $N_{\text{d}}$  values as high as those from the model have been observed elsewhere, for example within stratocumulus over the East China Sea (Koike et al., 2012). Therefore, this simulation represents

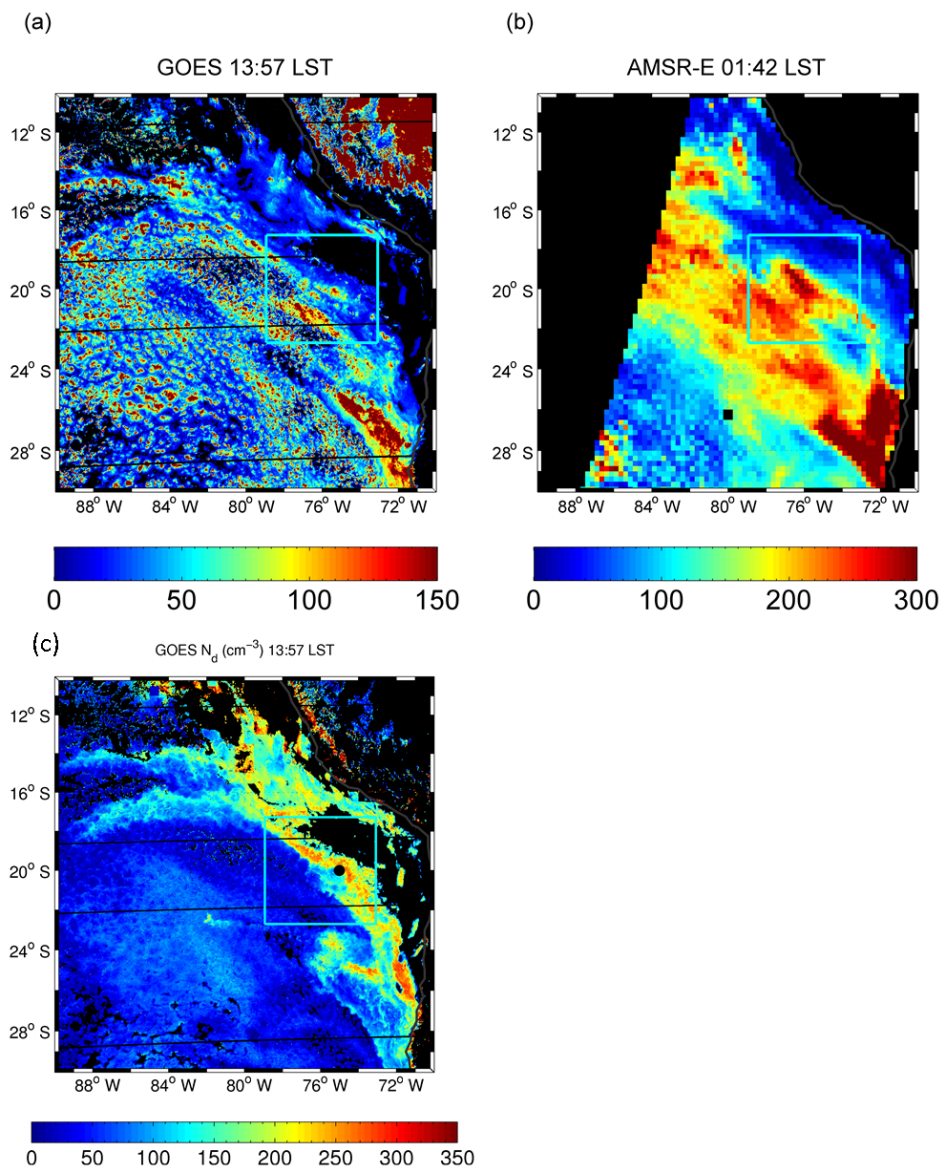


**Figure 2.** Snapshots of LWP (**a** and **b**,  $\text{gm}^{-2}$ ) and  $N_d$  (**c**) for 13 November 2008. (**a**) and (**c**) show 13:57 LST (daytime, 18:45 UTC) from the GOES-10 geostationary satellite at 4 km resolution. (**b**) Shows 01:42 LST (nighttime, 06:30 UTC) from the AMSR-E instrument that has a lower resolution of  $0.25^\circ$  (GOES-10 LWP and  $N_d$  retrievals are probably not reliable at nighttime). Note the different colour scales. The AMSR-E image has a region missing to the west due to the polar orbiting nature of the satellite and the limited swath width. Black regions in the LWP plots denote those where  $\text{LWP} < 20 \text{ gm}^{-2}$ , which we have chosen to define as cloud-free. The blue box shows the location of the 1 km resolution model domain.

the upper bound of  $N_d$  values that are likely to occur anywhere on earth. We will show later (e.g. Sects. 3.2.2 and 4.2) that the exact value for the upper bound of aerosol concentrations is not important given the lack of impact of aerosol on cloud properties as demonstrated by comparisons between the CASIM-Ndvar and CASIM-Ndvar-10 cases.

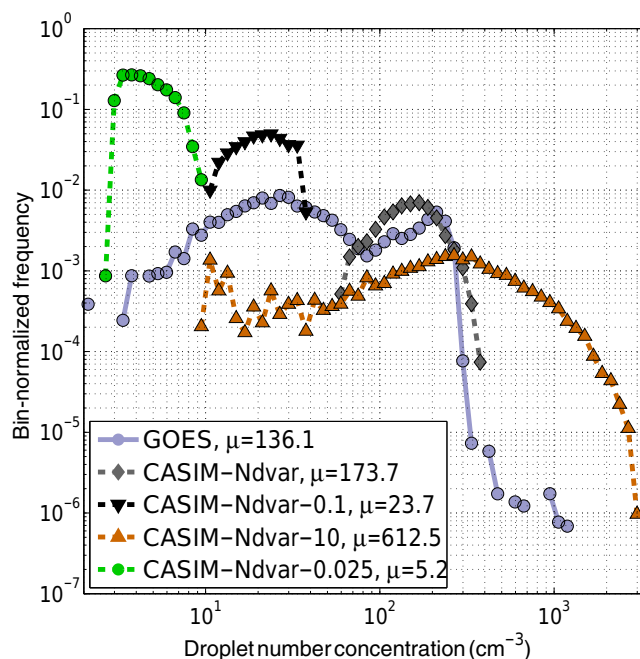
### 3.2.2 LWP and RWP time series

Figure 4 shows a time series of the mean LWP over the region of the UM domain for the different model simulations and the satellite observations. For the latter, both microwave instruments and GOES-10 retrievals are shown. There are several microwave instruments that give snapshots throughout the diurnal cycle. GOES-10 data are only used for the daytime, but give a higher time resolution. During the daytime, GOES-

**Table 5.** Details on the observations used in this study.

Instrument	Measurements used	Product	Product resolution	Native pixel resolution	Estimated error	Reference
Microwave radiometers (AMSRE, SSM/I-SSMIS, TMI, Windsat)	LWP (liquid water path)	Daily gridded	0.25°	~ 37 × 28 km for lowest-resolution instrument	2–3 g m <sup>-2</sup> (Lebock and Su, 2014)	www.remss.com
GOES-10	N <sub>d</sub> (droplet concentration)	VOCALS region data set	4 km	4 km	20 % mean low bias, <i>r</i> = 0.91, RMSE = 36 cm <sup>-3</sup> (Painemal et al., 2012)	Wood et al. (2011b)
GOES-10	LWP	VOCALS region data set	4 km	4 km	14.7 % mean high bias, <i>r</i> = 0.84, RMSE = 26.9 g m <sup>-2</sup> (Painemal et al., 2012)	Wood et al. (2011b)
CERES	LW and SW TOA fluxes	SSF Level-2 snapshots	20 km	20 km	5 % for SW, 3 % for LW (Loeb et al., 2007)	http://ceres.larc.nasa.gov/products.php?product=SSF-Level2
Microwave radiometer (shipborne; stationed at 20° S, 75° W)	LWP	Vertical profiles every 10 min	n/a	n/a	Unknown	Zuidema et al. (2005); de Szoeke et al. (2012)
W-band (94 GHz) radar (shipborne; stationed at 20° S, 75° W)	Radar reflectivity (DBZ)	Vertical profiles every 10 min	n/a	n/a	Unknown	Moran et al. (2011), de Szoeke et al. (2012), Parrill et al. (2014)

n/a = not applicable



**Figure 3.** PDFs of the cloud droplet number concentration for the model domain region. A snapshot time of 14:12 LST on 13 November is used for the model and 13:57 LST for the GOES-10 satellite, which is the nearest available data point. Three-dimensional model data are first converted to 2-D data, taking the  $N_d$  at the height of the maximum LWC with each model profile. The model data are subsequently coarse-grained from their native 1 km resolution to that of GOES-10 (4 km). Data points from both the model and the satellite are ignored if the LWP is less than 5 g m<sup>-2</sup>.

10 and the microwave instruments agree within  $\sim 10$  g m<sup>-2</sup>, giving confidence in the observations.

The model runs produce the observed peaks and troughs in LWP and even capture the secondary peak on 13 November at around 08:00 LST. The higher aerosol runs (CASIM-Ndvar and CASIM-Ndvar-10) and the old microphysics run (Old-mphys) also capture the magnitude of the LWP values well, although all simulations overestimate the daytime LWP values. There is better agreement for Old-mphys (overestimate of around 10 g m<sup>-2</sup>, or 10 %) than for the CASIM runs (overestimate of around 20–30 g m<sup>-2</sup>, or 50–75 %; however, note that the observed LWP is low at this time, being only 40 g m<sup>-2</sup>, resulting in a large percentage bias). The reverse is true for nighttime values where the CASIM runs match the observations very well (within 10 g m<sup>-2</sup>, or 10 %), but the Old-mphys run underestimates by 15–20 g m<sup>-2</sup>, or 15–20 %.

In the lower-aerosol runs (CASIM-Ndvar-0.1 and CASIM-Ndvar-0.025), LWP values are significantly lower, indicating a cloud macrophysical response via the precipitation rate. For the high-aerosol case, little impact of aerosol on the cloud field was found relative to the control case (CASIM-Ndvar). This is because little rain production occurs in the control case and hence the addition of more aerosol cannot have

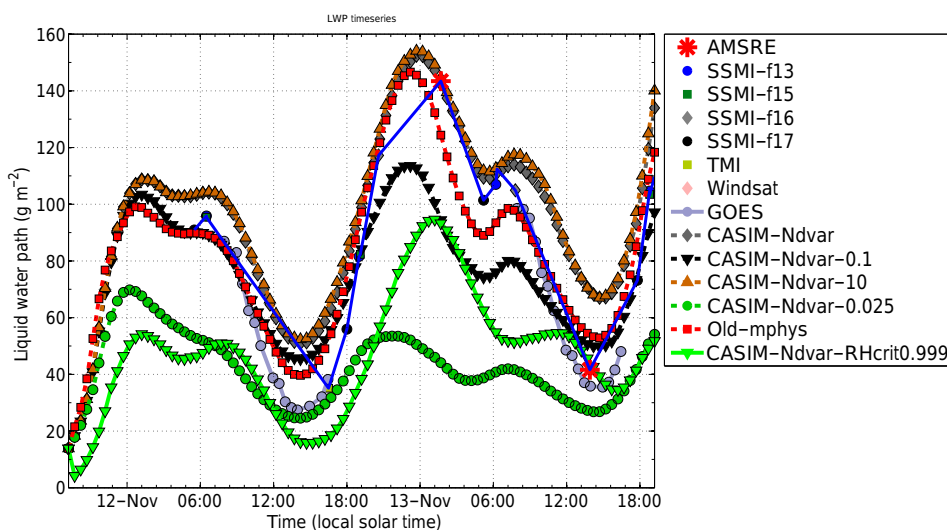


**Figure 4.** Time series of the mean LWP over the region of the UM domain for the different model simulations, the microwave satellite instruments, and the GOES-10 instrument. There are several microwave instruments that give snapshots throughout the diurnal cycle, as labelled in the legend; they are joined by the blue line. GOES-10 data are only used for the daytime, but they give higher time resolution. Retrievals where the solar zenith angle is larger than  $65^\circ$  have not been included due to likelihood of biases, as detailed in Grosvenor and Wood (2014).

much of a precipitation suppression impact. This is demonstrated in Fig. 5 where rainwater path (RWP) is between 8 and 11 times lower in the control case than in the lowest-aerosol case.

CASIM-Ndvar-RHcrit0.999 is a model run where the sub-grid cloud scheme has been switched off, which results in a very large LWP reduction compared to the control case, with LWP values similar to those from CASIM-Ndvar-0.025 for the first day and CASIM-Ndvar-0.1 for the second day. The results clearly highlight that while it is possible for the aerosol environment to have a large impact on the structure of the stratocumulus cloud deck (see CASIM-Ndvar-0.025 and CASIM-Ndvar), the role of the treatment of sub-grid humidity, even for grid spacings of 1 km, is still as important as a factor of 10–40 reduction in aerosol loading (see CASIM-Ndvar and CASIM-Ndvar-0.025 or CASIM-Ndvar-0.1). Given the unrealistically low LWP values in the CASIM-Ndvar-RHcrit0.999 case, the results from this run will not be included in future plots for clarity.

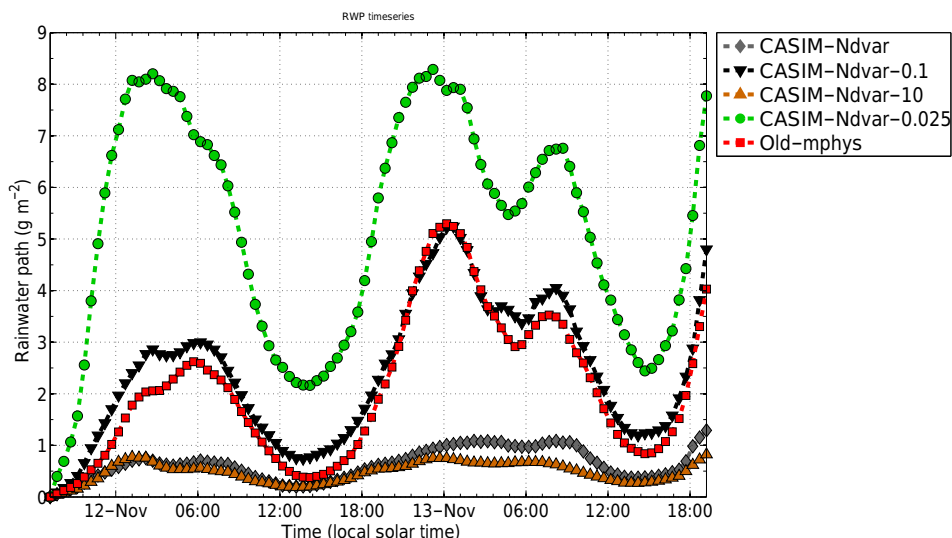
### 3.2.3 LWP maps and cloud coverage

Figure 6 shows the same daytime satellite LWP image from the GOES-10 satellite that was shown in Fig. 2, but zoomed in to the region of the model domain. Also shown are corresponding images from the control, very-low- and high-aerosol runs (CASIM-Ndvar, CASIM-Ndvar-0.025 and CASIM-Ndvar-10). The satellite image reveals that the clouds are orientated in diagonal-band-like structures of high LWP, and it also shows the structure of the POC regions, i.e. small regions of higher LWP (presumably the updraft region)

surrounded by regions of negligible cloud (downdraft–cold pool front region). There are two main POC regions within the model domain region: one centred at around  $19.75^\circ$  S,  $78.25^\circ$  W and another more elongated region centred at  $22.5^\circ$  S,  $76.75^\circ$  W, but stretching to the NW and SE.

The control and high-aerosol simulations qualitatively represent the diagonal band structures and the low LWP values near the coast (in the NE corner of the domain) very well, despite the fact that there is no spatial gradient in the aerosol field of the model, as there would be in reality. This indicates a general dominance of the meteorological state over the macrophysical properties of the clouds. However, in the very-low-aerosol run (CASIM-Ndvar-0.025), LWP values and the cloud fraction are significantly lower, indicating a cloud macrophysical response via the precipitation rate, which is similar to what has been observed in LES studies (Berner et al., 2013; Feingold et al., 2015). For the high-aerosol case, little impact of aerosol on the cloud field was found relative to the control case. This is because precipitation is low in the control case (Fig. 5) and so the addition of more aerosol cannot influence precipitation.

The CASIM-Ndvar and CASIM-Ndvar-10 cases display some clear regions in between the diagonal bands of high LWP, but they are much smaller than the observed POC regions. The low-aerosol run produces small-sized convective cells surrounded by clear air that are reminiscent of the observed POC regions, but they occur throughout the whole domain. Thus, this suggests that the model is capable of producing open-cell features given low enough aerosol concentrations, but cannot reproduce isolated POC regions in amongst the closed-cell convection.



**Figure 5.** As for Fig. 4, except for RWP and for the models only.

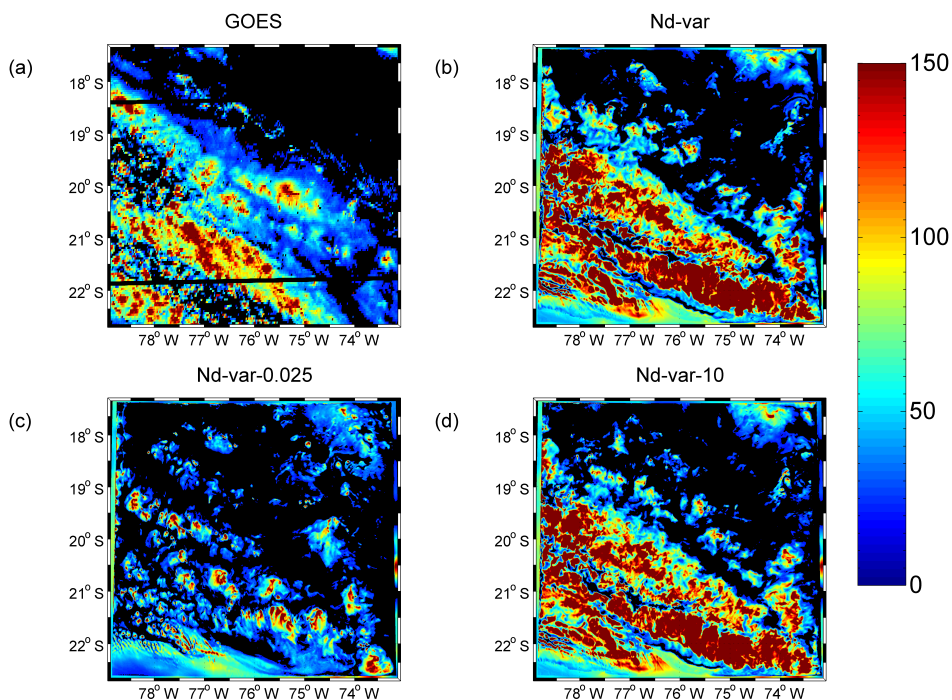


**Figure 6.** Daytime snapshots of LWP ( $\text{g m}^{-2}$ ) for 13 November 2008 for the region of the inner model domain. (a) GOES-10 satellite at 13:57 LST (daytime); (b) model with control aerosol; (c) model with  $\times 0.025$  aerosol; (d) model with  $\times 10$  aerosol. The model images are from 14:12 LST. Regions where the LWP is less than  $20 \text{ g m}^{-2}$  are plotted as black to give an estimate of cloud fraction.

The nighttime LWP maps in Fig. 7 show that a large area of high-LWP cloud is observed by AMSR-E. The CASIM-Ndvar and CASIM-Ndvar-10 models also produce a large region of high-LWP cloud in the southwest corner of the domain, but this is less widespread than observed and reaches higher LWP values. As for the daytime, there is little response between the CASIM-Ndvar and CASIM-

Ndvar-10 cases, but a large response when aerosol is reduced (CASIM-Ndvar-0.025), again with lower LWPs and lower cloud fractions that are similar to open-cell stratocumulus.

### 3.2.4 LWP distributions

Figure 8 shows PDFs of LWP from the model and satellite for the periods surrounding the daytime minima in LWP (10:00–

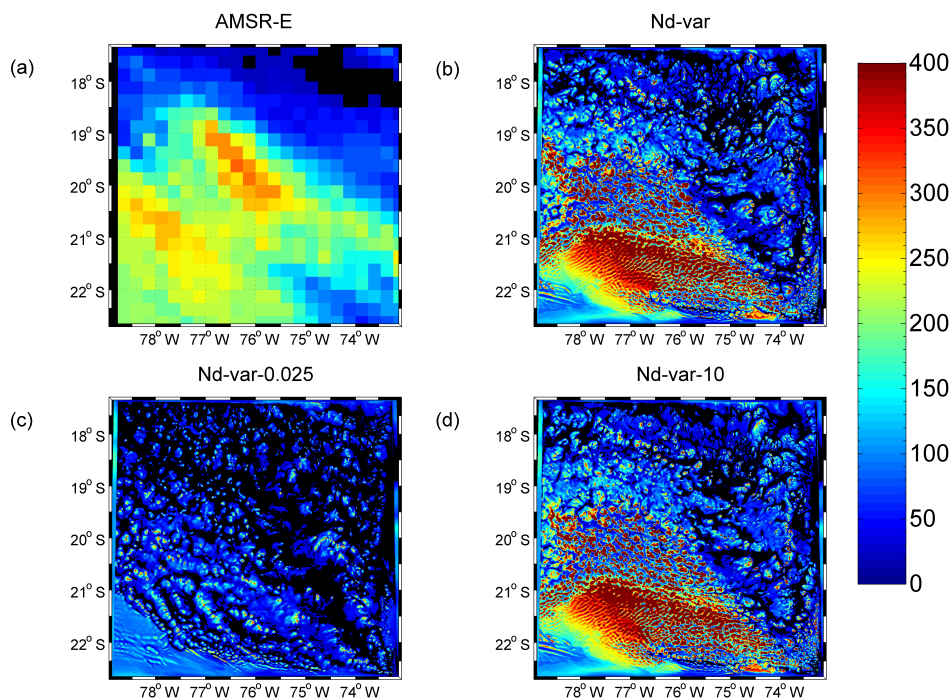


**Figure 7.** As for Fig. 6, except for nighttime (01:42 LST for AMSR-E and 02:12 LST for the model).

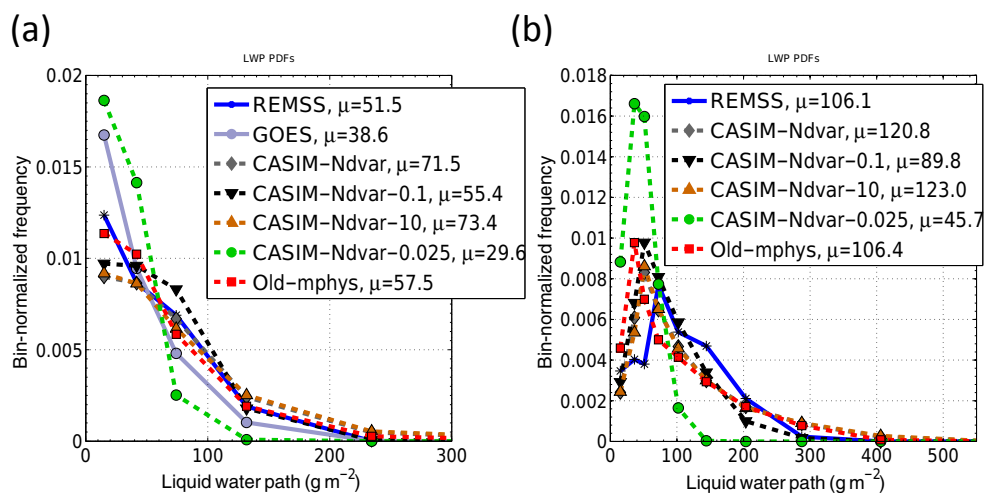


**Figure 8.** PDFs of LWP for daytime (left) and nighttime (right) time periods for the model and for satellite observations. “REMSS” refers to the several available REMSS microwave instruments, each of which provides a snapshot LWP field. For the daytime, the times surrounding the minima in the LWP diurnal cycle (see Fig. 4) are used (10:00–18:00 LST on both 12 and 13 November; overall four REMSS snapshots). For the nighttime, only the REMSS satellites are shown; times are chosen surrounding the maxima of the LWP cycle, but the surrounding period is reduced compared to the daytime in order to match the limited available REMSS times as closely as possible (03:00–09:00 LST on 12 November, 20:00 LST on 12 November to 10:00 LST on 13 November, 18:30–20:00 LST on 13 November; contains nine REMSS snapshots). The model and GOES-10 data have been coarse-grained to the AMSR-E resolution of  $0.25^\circ$ .

18:00 LST on 12 and 13 November) from both the REMSS microwave instruments (hereafter referred to as REMSS) and GOES-10. There is some disagreement between GOES-10 and REMSS, with GOES-10 generally producing more low LWP values (and fewer high ones). This could indicate obser-

vational uncertainty; however, sampling bias due to the less-frequent REMSS observations is more likely since the mean values between GOES and REMSS generally agree well for the same times (see Fig. 4). The control (CASIM-Ndvar) and high-aerosol (CASIM-Ndvar-10) cases show generally

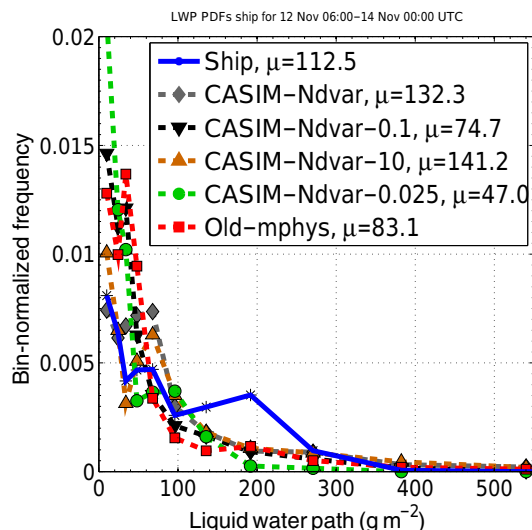


**Figure 9.** PDFs of LWP for the period from 06:00 UTC on 12 November to 00:00 UTC on 14 November 2008 from the RV *Ronald H. Brown* microwave radiometer and various UM model runs. For both the ship and the model, 10 min averaged data are used. For the model the  $3 \times 3$  grid boxes centred at the location of the ship ( $20^\circ$  S,  $75^\circ$  W) are used and combined into one PDF in order to account for the possibility of spatial variability.

good agreement with the observations, although frequencies are too low for the lowest LWP bin centred at  $15 \text{ g m}^{-2}$  and slightly too high for LWP values  $> \sim 60\text{--}100 \text{ g m}^{-2}$ , which is consistent with the overprediction of the mean LWP (Fig. 4). This is especially true when comparing to GOES. The CASIM-Ndvar-0.1 and Old-mphys runs are quite similar to each other and both exhibit less underprediction of the low LWP values than the CASIM-Ndvar and CASIM-Ndvar-10 runs. The CASIM-Ndvar-0.025 run has too few high LWP points and too many low ones, again consistent with the underprediction of mean LWP for this run compared to the observations.

Also shown are nighttime LWP PDFs from the REMSS satellites only. The models all show some degree of underestimate for LWP values at around  $130 \text{ g m}^{-2}$  and have frequencies that are too high at lower LWPs of around  $30\text{--}100 \text{ g m}^{-2}$ , but with the CASIM-Ndvar and CASIM-Ndvar-10 runs showing less overprediction than the other runs. As demonstrated for the daytime, the CASIM-Ndvar-0.025 run has a much larger number of low LWP values compared to the observations and the other models, indicating excessive LWP removal by precipitation. Consistent with this, the higher-aerosol runs (CASIM-Ndvar and CASIM-Ndvar-10) and the Old-mphys run have a small number of points with LWP larger than around  $300 \text{ g m}^{-2}$ , which are not present for the low-aerosol runs (CASIM-Ndvar-0.025 and CASIM-Ndvar-0.1). There are also higher frequencies of the higher LWP values in the CASIM-Ndvar-0.1 case compared to the CASIM-Ndvar-0.025.

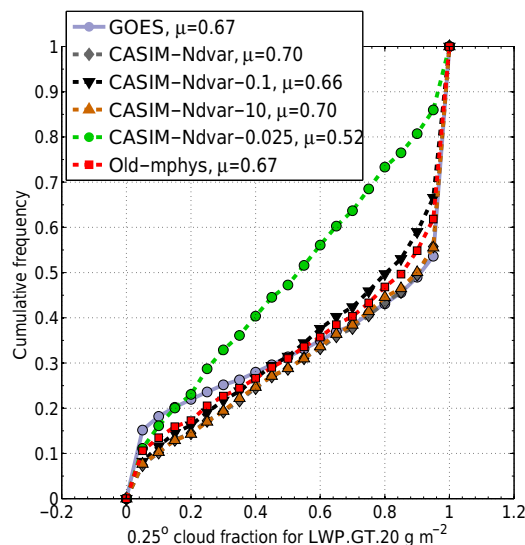


**Figure 10.** Cloud fraction cumulative distribution functions between 08:12 and 16:12 LST for the model and 07:57 and 15:57 for GOES-10 sampled every 30 min. Here each cloud fraction value is calculated as the fraction of data points with LWP greater than  $20 \text{ g m}^{-2}$  relative to the total number of data points in  $0.25^\circ \times 0.25^\circ$  areas. GOES-10 data are used at the native 4 km resolution and the model LWP data are first coarse-grained to this resolution from the native 1 km resolution.

In addition to spatial satellite PDFs, the microwave radiometer onboard the RV *Ronald H. Brown* can provide a measure of temporal variability at a resolution of 10 min, but at a fixed location ( $20^\circ$  S,  $75^\circ$  W). Figure 9 shows LWP PDFs from the ship and for various model runs for the time period 06:00 UTC (01:12 LST) 12 November to 00:00 UTC on 14 November (19:12 LST on 13 November). A long sampling period is necessary given the restriction of the ship sampling being at only one location.

Figure 9 shows that all of the models underestimate the occurrence of LWP  $> 150 \text{ g m}^{-2}$  values and overestimate the occurrence of the lower LWP values for this region (LWP  $< 50\text{--}100 \text{ g m}^{-2}$  depending on the model run). However, the overestimate of the low values is much less severe for the CASIM-Ndvar and CASIM-Ndvar-10 runs. These results are consistent with the REMSS nighttime results from Fig. 8.

### 3.2.5 Distributions of cloud fraction

Figure 10 shows distributions of cloud fraction ( $f_c$ ) for the model runs and for the GOES-10 satellite for the entirety of the daytime period of 13 November (between approximately 08:00 and 16:00 LST). For the cloud fraction calculation, the model LWP data are first coarse-grained to the GOES-10 resolution of 4 km and then the cloud fraction is defined within  $0.25^\circ$  regions based on a LWP threshold of  $20 \text{ g m}^{-2}$ .

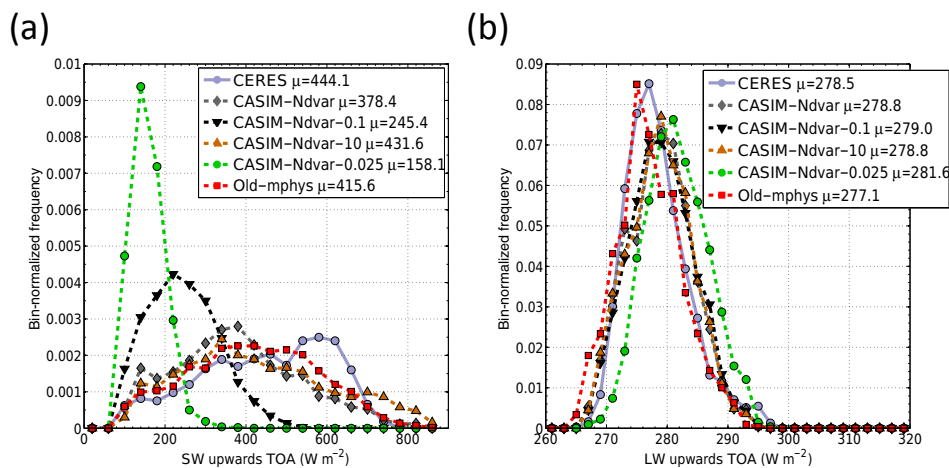


**Figure 11.** Shortwave (left) and long-wave (right) top of the atmosphere radiative flux PDFs from CERES and the model for daytime periods for the region of the model domain. This is a combined PDF from the three separate snapshot overpass times of the CERES satellite for the model domain that were available for the simulation period: 10:24 LST (15:12 UTC) on 12 November (Terra satellite), 14:19 LST (19:06 UTC) on 12 November (Aqua satellite), and 11:07 am LST (15:55 UTC) on 13 November (Terra). For the model, the three closest available times were used: 15:00 and 19:00 UTC on 12 November 16:00 UTC on 13 November. Note that CERES–Aqua data are not available for the afternoon (local time) of 13 November. The model data were first coarse-grained to 20 km, which is the approximate resolution of the CERES data.

Figure 10 shows agreement between the model and observations to within 0.1 in terms of cloud fraction for all of the runs, except for the lowest aerosol case (CASIM-Ndvar-0.025), suggesting that the model is very capable of correctly simulating the balance of cloudy and cloud-free areal coverage. For the model runs (excluding the lowest aerosol  $\mu$  case) and the observations, the  $f_c$  bin that contributes most to the frequency is the highest  $f_c$  value ( $> 0.95$ ), corresponding to nearly overcast conditions. The Old-mphys and CASIM-Ndvar-0.1 runs both have similar contributions to the frequency from this bin, as well as for other  $f_c$  values at the upper end of the distribution, with both underestimating the contribution to the total compared to the observations (i.e. these models do not have enough of the higher  $f_c$  values). In contrast, the CASIM-Ndvar and CASIM-Ndvar-10 agree with the observations to within  $\sim 0.04$  cloud fraction for  $f_c > 0.7$ . Thus, CASIM microphysics with the sub-grid cloud scheme seem to represent an improvement over the old microphysics in this aspect.

The low-aerosol case (CASIM-Ndvar-0.025) showed a much greater frequency of the lower cloud fractions and very few fully overcast data points, which is consistent with the results and discussion of the snapshot maps (discussed above).

A distribution plot is not possible for the nighttime where only coarse resolution ( $0.25^\circ$ ) snapshots from the microwave instruments are available. The domain-average cloud fraction using the same  $20 \text{ g m}^{-2}$  LWP threshold was 0.95 for the AMSR-E satellite image (Fig. 7), which is very similar to that predicted in the control and high-aerosol cases (0.97 and 0.98 respectively after coarse graining to  $0.25^\circ$ ). Again, the very-low-aerosol case (CASIM-Ndvar-0.025) showed the

tendency to produce a much lower cloud fraction (0.79). Thus, the model shows large sensitivity of the cloud coverage to aerosol for the entirety of the daytime period and likely for the nighttime period too.

### 3.2.6 Radiative flux distributions

Figure 11 shows PDFs of the shortwave and long-wave top-of-the-atmosphere (TOA) fluxes from CERES and the models for the region of the model domain (hereafter  $\text{SW}_{\text{upTOA}}$  and  $\text{LW}_{\text{upTOA}}$  respectively). The results show that the aerosol amount has a large influence on the shortwave (SW) fluxes, with the CASIM-Ndvar-0.1 and CASIM-Ndvar-0.025 runs showing mode fluxes that are much lower than those observed by CERES. The other runs produce SW distributions that are very similar to the those observed with CERES. The low values in the CASIM-Ndvar-0.1 run are unlikely to be the result of cloud fraction differences since Fig. 10 showed similar distributions for this and the higher aerosol runs. Instead, the response of the SW flux results from the marked change in LWP when aerosol is changed (Fig. 4) and from the change in  $N_d$  (Fig. 3); this attribution is discussed in more detail in Section 4.3. There is a shift in the long-wave (LW) flux towards higher fluxes relative to the control case for CASIM-Ndvar-0.025, but not for CASIM-Ndvar-0.1. This shift is due to the cloud fraction response seen in CASIM-Ndvar-0.025, but not in CASIM-Ndvar-0.1 (Fig. 10); a lower cloud fraction will mean larger LW fluxes due to CERES detecting radiation emitted from more surface points with correspondingly warmer temperatures.

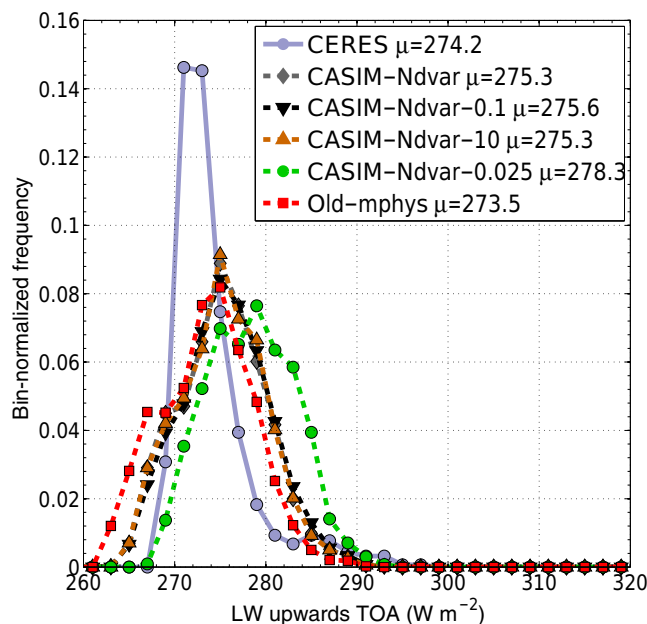
The CASIM-Ndvar, CASIM-Ndvar-10 and Old-mphys runs all produce SW and LW distributions that are relatively close to those observed. There are a few discrepancies for the SW fluxes such as the observed peak in frequencies between 500 and 700  $\text{W m}^{-2}$  not being captured by the models, which show correspondingly larger peaks at lower SW values. PDFs of the LW CERES overpasses for the model and GOES-10 (not shown) suggest that the error is attributable to an underestimate in the number of  $N_d$  values between around 210 and 300  $\text{cm}^{-3}$ . The Old-mphys run has  $N_d$  fixed at 100  $\text{cm}^{-3}$ . For LW the Old-mphys run has values that are shifted slightly towards lower LW values compared to the other runs, which agrees with the observations better than the CASIM runs for the upper tail of the distribution, but not as well for the lower tail. The modal value of the CASIM runs is also slightly too high compared to the observations, whereas the mode for Old-mphys is slightly too low. The mean values of the CASIM-Ndvar, CASIM-Ndvar-0.1 and CASIM-Ndvar-10 runs agree with CERES within 0.2 %, with the Old-mphys and CASIM-Ndvar-0.025 runs performing slightly worse ( $-0.5$  and  $+1.1$  % biases respectively).

Figure 12 shows the equivalent plot, but for nighttime snapshots. The models generally all produce distributions that are shifted to too-high LW flux values, indicating either clouds that are too low in altitude, cloud fractions that are too low, or clouds that are too thin. However, we note that cloud thickness would only be relevant for very thin cloud regions ( $< \sim 20 \text{ g m}^{-2}$ ) since the increase in LW flux with LWP saturates at low LWP values (Miller et al., 2015). As for the daytime results, there is a much greater shift to high values for the CASIM-Ndvar-0.025 run, indicating the lesser cloud coverage in this case. The Old-mphys run is shifted to slightly lower values compared to the other runs as was also the case for the daytime LW fluxes. Again, Old-mphys agrees better than the other runs for the upper tail of the observations, but not for the lower tail, which is representative of cloud top conditions.

### 3.2.7 Thermodynamic profiles

Regular radiosondes were released from the RV *Ronald H. Brown*, allowing a comparison of the model to observations for thermodynamic profiles. Figure 13 shows this comparison for the potential temperature ( $\theta$ ) and water vapour mixing ratio ( $q_v$ ) for the control run only (CASIM-Ndvar); except for  $q_v$  for the CASIM-Ndvar-0.025 run, all of the runs showed very similar results and so are not shown. CASIM-Ndvar-0.025 was likely anomalous due to the lack of cloud cover in that run. Three times are shown that are close to the peaks and troughs of the diurnal cycle of LWP (see Fig. 4), but excluding the first peak at 03:00 LST on 12 November to allow for model spin-up.

For the first time shown (15:55 LST on 12 November, i.e. daytime), the  $\theta$  profile from the model matches that ob-



**Figure 12.** As for Fig. 11, except for nighttime periods and for long-wave only. The times used for CERES are 22:35 LST (03:23 UTC) on 12 November (Terra satellite), 02:39 LST (07:27 UTC) on 12 November (Aqua satellite), and 01:44 am LST (06:32 UTC) on 13 November (Aqua). For the model, the three closest available times were used: 03:30 and 07:30 UTC on 12 November; 06:30 UTC on 13 November.

served almost exactly, including the height of the sharp inversion, but the  $q_v$  profile is around  $1 \text{ g kg}^{-1}$  too moist in the boundary layer. The decrease in  $q_v$  associated with the inversion is also not as sharp as in reality. The model biases for both of the other two times shown (13 November; nighttime, 03:29 LST; daytime, 15:09 LST) are similar to each other. In the model boundary layer, the modelled  $\theta$  and  $q_v$  agree with reality within 1 K and  $0.5 \text{ g kg}^{-1}$  respectively, but the sudden changes associated with the inversion are too low by around 200 m. Above the inversion the model is also too warm by a maximum of around 3 K and slightly too moist in the region 500–600 m above the inversion by a maximum of approximately  $1 \text{ g kg}^{-1}$ . Overall, the results suggest that the model matches reality very well in terms of the thermodynamic conditions, except for a tendency for the inversion to be too low by around 200 m.

### 3.2.8 Radar reflectivity

Also onboard the RV *Ronald H. Brown* was a W-band radar, which provided vertical profiles of radar reflectivity (dBZ). This is useful for evaluating the vertical placement of cloud in the model as well as helping to assess the amount of rain formation and its vertical distribution. Figure 14 shows 2-D PDFs of the ship and model radar reflectivity vs. height. Model data are used from all of the grid points in the  $1^\circ \times 1^\circ$

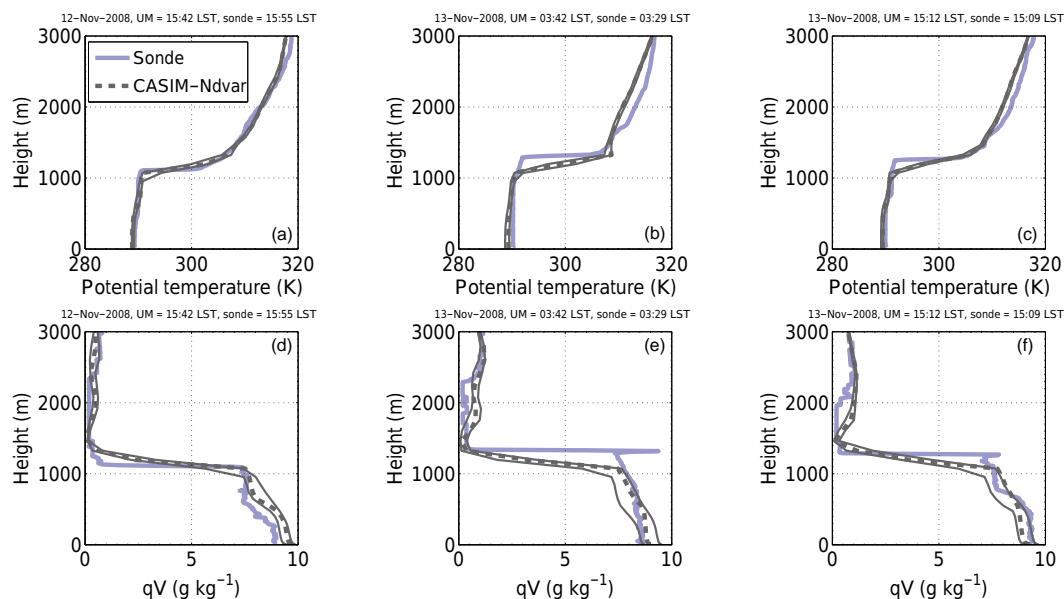


**Figure 13.** Profiles of potential temperature (top row) and water vapour mixing ratio (bottom row) from radiosondes released from the RV *Ronald H. Brown* (labelled “sonde”) and from the control UM run (CASIM-Ndvar). Three different radiosonde times are shown; 15:55 LST on 12 November (left), 03:29 LST on 13 November (middle), and 15:09 LST on 13 November (right), with the closest available UM time being used (see titles of each sub-plot). The closest profile in the UM to the ship location is shown as the dashed grey line and the surrounding thin grey lines show the 10th and 90th percentiles at each height from all of the profiles in a  $1^\circ \times 1^\circ$  region around the ship.

region that surrounds the ship location to compute radar reflectivity based on Rayleigh scattering. Tests using smaller sampling regions (down to  $3 \times 3$  km; not shown) show very little change in the patterns of frequencies for the 2-D PDFs, indicating that the choice of sampling scale is not very important for this comparison. The ship radar results show a single mode of reflectivity up to values of around  $-4$  dBZ that likely represent cloud droplets or small drizzle rather than larger rain droplets since model data in BA12 suggested that rain would appear as a separate mode at higher reflectivity values between around  $-10$  and  $+10$  dBZ. Most of the data points lie above 550 m in altitude, although there are some data from lower altitudes and there is a strong mode centred at 1135 m and  $-24$  dBZ. The cloud reflectivity generally grows with altitude up to around 1 km, which is consistent with the growth of cloud droplets from above cloud base. Above this height the reflectivity starts to reduce; this could signify the evaporation of cloud due to the entrainment of dry, free tropospheric air into the upper regions of the clouds (A04), which could reduce reflectivity through changes in droplet size, number, or both. Alternatively, it may be the result of the presence of less drizzle near the top of the cloud. Most of the observed cloud is below 1325 m in altitude, although some cloud was observed up to 1460 m (within the accuracy of the height bins). It is likely that this corresponds closely with the boundary layer height because cloud tops for stratocumulus generally correspond with the inversion height.

The CASIM-Ndvar (control model) and CASIM-Ndvar-10 model results are similar to each other, but show some significant differences compared to the observations. The cloud from the model does not extend much above 1200 m, in contrast to the observed cloud reaching 1460 m. This height difference corresponds to approximately two model levels at these altitudes. Also, the model reflectivities do not tend to reduce with height towards the cloud top as they do in reality. The model also has a higher frequency of points at lower altitudes compared to the observations, e.g. the maximum height of the  $3 \times 10^{-3}$  frequency contour is 693 m for the observations and 293 m for the model. This leads to an overall cloud depth (as calculated using the frequency contour above) of 767 m for the observations and 907 m for the model (an 18 % overestimate). In the region of the lower-altitude cloud in the model, there is also a higher frequency of lower reflectivity values in the range  $-40$  to  $-20$  dBZ than is observed.

However, there are also some similarities; both the models and the observations show a general increase in reflectivity in the lower regions of the clouds, with a vertical gradient that is similar to that observed. Also, the highest dBZ values reached (99.9th percentile of all data, including cloud free regions) were around  $-5.2$  dBZ for the observations, whereas for the model the equivalent values were  $-1.9$ ,  $-6.7$ , and  $+7.4$  dBZ for the CASIM-Ndvar, CASIM-Ndvar-10 and CASIM-Ndvar-0.025 runs respectively. Thus, the maximum droplet and raindrop embryo sizes reached in the model were close to those in reality for the CASIM-Ndvar and CASIM-

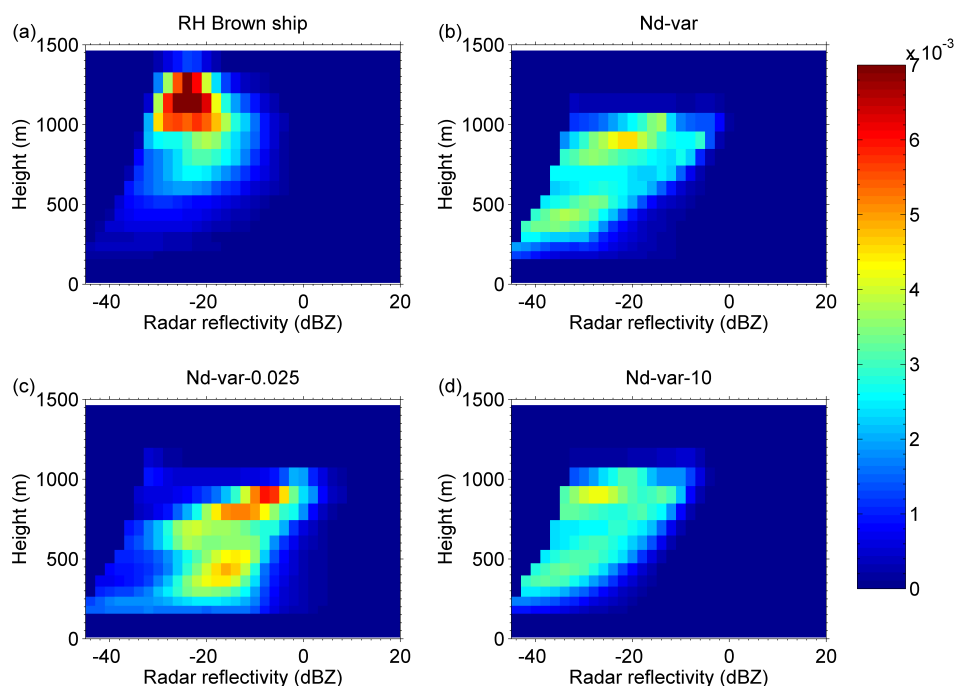


**Figure 14.** Two-dimensional relative frequency plot for radar reflectivity vs. height from the RV *Ronald H. Brown* W-band radar and for various model runs. The relevant model data are available every 30 min and data between the times of 06:00 UTC (01:12 LST) on 12 November and 00:00 UTC (19:12 LST) on 14 November are used, with the first 6 h of model data being avoided due to spin-up. Ship radar profiles are available every 0.3 s and are used for the same time period as the models. Model data are used for the  $1^\circ \times 1^\circ$  region around the location of the ship. The colours indicate the normalized frequency of occurrence for each bin and the ship and model bin sizes are the same. Note that many of the data points lie beyond the minimum value on the  $x$  axis (i.e. very low radar reflectivity) and are not visible, but they are included for the normalization. The ship radar has a minimum detectable reflectivity that increases with height; model data below this height-dependent threshold were set to  $-1000$  dBZ.

Ndvar-10 cases. In the CASIM-Ndvar-0.025 case the low aerosol concentrations allow larger droplets to form.

#### 4 Discussion

A kilometre-scale regional model using cloud aerosol interacting microphysics has been used to simulate stratocumulus in the SE Pacific. It was seen that the introduction of the treatment of subgrid humidity (the cloud scheme) was important for simulating the observations. The range of aerosol loading used in the sensitivity studies resulted in droplet concentrations that included the observed range and captured extreme conditions for stratocumulus cloud. This provided insight into the relative importance of cloud brightening versus macrophysical changes such as cloud cover and LWP, which will be discussed further in this section.

#### 4.1 Can a regional model produce a realistic representation of stratocumulus cloud when compared to a diverse range of observations?

We have shown that the UM regional model with the sub-grid cloud scheme reproduced many important physical observations for the control case. The shape and magnitude of the observed diurnal cycle of domain mean LWP was captured to within  $\sim 10 \text{ g m}^{-2}$  for the control run for the nighttime, but with an overestimate for the daytime of up to  $30 \text{ g m}^{-2}$ . The shapes and sizes of the observed bands of clouds were (qualitatively) reproduced and the model simulated open-cell-like regions of low areal cloud cover to the NE of the domain and cloudy bands in the SW in between (Fig. 6). The daytime cloud fraction ( $f_c$ ) frequency distribution, especially for the larger cloud fraction values ( $f_c > \sim 0.7$ ) was reproduced to within a  $\Delta f_c$  of 0.04, as was the domain mean nighttime  $f_c$  at a single time (to within a  $\Delta f_c$  of 0.02). Frequency distributions of shortwave and long-wave TOA fluxes were close to those from observations; the means were underestimated by 15 and 0.4 % respectively. The higher of the two observed modes of the frequency distribution of droplet number concentrations was reproduced in the control case with the mode

value agreeing to within  $\sim 20\%$ . Also, the good comparison (to within  $\sim 15\%$ ) of the width of the droplet concentration distribution indicates a good representation of model updraft velocities and the physics of the aerosol activation process, although we also acknowledge that the aerosol mass and number concentrations in the control model run were uniformly scaled to approximately match the observed droplet concentrations.

Thus, there is good evidence that the model correctly captures the physical processes that are of first-order importance for producing a realistic stratocumulus deck. However, there are some model deficiencies, which we now discuss, that were highlighted in the comparison to the observations.

Section 3.2.2 detailed how the daytime control run had a tendency to overestimate the LWP, particularly at the times of the lowest observed LWP. Examination of the daytime PDF of LWP (Fig. 8a) revealed a slight lack of LWP values between around 15 and  $70\text{ g m}^{-2}$  and too many of the higher LWP ( $> \sim 125\text{ g m}^{-2}$ ) values. A similar problem occurs at night (Fig. 8b), with a lack of LWP values between 150 and  $250\text{ g m}^{-2}$  and was also evident from the comparisons to the longer-term (day and night combined) single-location ship observations (Fig. 9). This overestimation of LWP may be related to the lack of a lower mode of modelled  $N_d$  values, which is evident from the  $N_d$  PDF (Fig. 3). It is likely that the presence of the low- $N_d$  mode in reality caused LWP removal through precipitation, which would lead to a reduction in the higher LWP values. The latter occurred in the lower-aerosol runs in the model (CASIM-Ndvar-0.1 and CASIM-Ndvar-0.025), which were closer to the observed frequencies for the highest LWP values, and so if the lower-observed- $N_d$  mode was present in the control model case (along with the higher mode), then we would expect the match to observations to improve. The dual mode of  $N_d$  that was observed in reality could have been the result of a spatial gradient in  $N_d$  (Fig. 2c), which is not captured by the model since we employ a uniform aerosol field. The introduction of a spatial aerosol gradient or the use of a realistic aerosol model that simulates the aerosol sources, transport, and chemical transformation may rectify this problem.

BA12 found a similar daytime overestimate of LWP, but were only considering the near-coastal region where the ship was located. The reason for this was attributed to the sub-grid cloud scheme, which created too much cloud when supplied with the observed thermodynamic profiles. Since we use the same cloud fraction approach as BA12, albeit linked to a different microphysics scheme, this may also be an issue in this work. However, we note that the run with the old microphysics scheme (Old-mphys), which will be similar to the runs in BA12 since the same microphysics and cloud schemes are used, shows a domain-mean LWP value that is quite similar to that observed at the time of the daytime minima. This suggests that the overestimate in the near-coastal region that was observed in BA12 does not have a large impact on the overall domain mean. In addition, Fig. 4 clearly

shows that the aerosol concentration has an impact on the LWP at this time, with lower aerosol concentrations reducing the LWP significantly.

Another issue with the model was that the cloud-top heights were too low compared to shipborne radar observations (Fig. 14). This is consistent with the results from Sect. 3.2.7 and BA12 where the UM model boundary layer height was found to be too low for this case through comparisons to radiosondes released from the ship, and it is also consistent with Abel et al. (2010) where the UM boundary layer height was on average  $\sim 200\text{ m}$  too low during the VOCALS field campaign period for NWP configuration runs at  $0.15^\circ$  resolution. BA12 found that an improved treatment of rain microphysics increased the height of the boundary layer in their 1 km resolution nest through the suppression of precipitation. The improvements led to increased instances of coupled boundary layers as diagnosed by the boundary layer scheme. In our case, though, the boundary layer is too low even in the very-high-aerosol case (CASIM-Ndvar-10) when precipitation has already been completely suppressed, indicating that this is not the cause of the low boundary layer in our runs. The most likely source of this discrepancy is the meteorology of the global driving model, which imposes an initial capping inversion on the 1 km nest that is too low. This could be reinforced through the lateral boundary conditions, which might prevent the inner nest from growing its boundary layer through entrainment. Another possibility is that both the global model and the inner nest do not produce enough entrainment, which then leads to boundary layers that are too low. This is consistent with the results that are discussed in Sect. 4.2, whereby the modelled LWP in the high-resolution nest does not decrease at very high aerosol concentrations.

The fact that the modelled boundary layer height was too low is also consistent with the overestimate of the LW TOA upwards fluxes during both the daytime and the nighttime (Figs. 11 and 12) since it would correspond to cloud-top temperatures that were too large. It is possible that the LW TOA overestimate is also indicative of a cloud fraction that is too low, meaning that more surface points contribute. However, this seems less likely given that the cloud fraction generally agreed well with the observations during both the daytime and the nighttime, although we note that the nighttime comparison of cloud fraction is limited to a single time.

The results presented in this paper suggest that the UM regional model with a relatively coarse horizontal and vertical resolution (1 km and  $\sim 100\text{ m}$  at the top of the boundary layer respectively) can reproduce most of the observed cloud characteristics for the case presented and thus produces a realistic representation of stratocumulus clouds. However, we also emphasize that a good agreement was only found when employing a sub-grid cloud scheme to represent sub-grid variability in relative humidity. This is discussed further in Sect. 4.4.

## 4.2 How do the modelled clouds respond to aerosol?

Figure 15 summarizes the response of various domain- and time-mean cloud properties to cloud droplet concentration ( $N_d$ ), with the  $N_d$  changes being driven by aerosol changes. The mean  $SW_{\text{upTOA}}$  increases monotonically with  $N_d$  with the value for CASIM-Ndvar-10 being more than twice that in CASIM-Ndvar-0.025. The other cloud properties show a non-monotonic increase across all  $N_d$  values. Both the domain-mean LWP and the in-cloud LWP ( $LWP_{\text{ic}}$ , cloudy regions defined as  $LWP > 20 \text{ g m}^{-2}$ ) increase at lower  $N_d$  values with respectively 84 and 52 % increases between the CASIM-Ndvar-0.025 and CASIM-Ndvar cases when the aerosol was increased by a factor of 40. In contrast, there was very little increase in LWP between the CASIM-Ndvar and CASIM-Ndvar-10 cases when the aerosol was increased by a factor of 10.

This variation in response is due to the influence of aerosol on the suppression of rain. As shown in Fig. 15, at low  $N_d$  rain production (RWP) is relatively large; thus, increasing aerosol leads to a reduction in rain production and an increase in LWP. When the mean  $N_d$  reaches around  $200 \text{ cm}^{-3}$  (CASIM-Ndvar case), rain production has almost completely shut off; thus, any further increases in  $N_d$  have no impact on LWP. Such behaviour is consistent with high-resolution LES studies (e.g. A04). The simulations presented here show that a coarser-resolution NWP model can simulate this behaviour. We also note that in some of the situations examined in A04, when  $N_d$  was increased from very low to high levels they simulated a similar proportional increase in LWP to that which we observe between the CASIM-Ndvar-0.025 and CASIM-Ndvar runs.

The simulations in A04 also showed that once precipitation had been completely suppressed, LWP tended to decrease, with further  $N_d$  increases due to entrainment effects related to the ever-smaller droplet sizes (Bretherton et al., 2007; Hill et al., 2009). However, we do not see such behaviour in our model in test runs (not shown) of the CASIM-Ndvar and CASIM-Ndvar-10 cases that include droplet sedimentation as a function of droplet size. This suggests that the entrainment parameterization within the boundary layer scheme (Lock et al., 2000) may need refinement to become more sensitive to the cloud droplet number concentration. Enhanced vertical resolution near the cloud top would also undoubtedly improve the explicit representation of the entrainment interface layer, but such sensitivities are out of the scope of this study.

### 4.2.1 Cloud fraction response

Cloud fraction generally only increases between the CASIM-Ndvar-0.025 and CASIM-Ndvar-0.1 runs, indicating that the change in LWP between those runs is due to an increase in both  $f_c$  and  $LWP_{\text{ic}}$ . No major increase in  $f_c$  occurs between the CASIM-Ndvar-0.1 and CASIM-Ndvar cases, whereas

there is a fairly large increase in  $LWP_{\text{ic}}$  (27 %), indicating cloud thickening.

Thus, the cloud fraction exhibits a step change, which only occurs at very low  $N_d$  values (mean values  $< 30 \text{ cm}^{-3}$  in our simulations). Such behaviour makes it questionable whether aerosol cloud metrics where the response of cloud fraction to  $N_d$  or aerosol is defined in terms of  $d\log(f_c)/d\log(N_d)$  (e.g. Quaas et al., 2010, albeit this study used aerosol optical depth instead of  $N_d$ ) is appropriate, at least across a wide range of  $N_d$  values. The addition of aerosol processing to our model will alter this behaviour somewhat, with the likelihood being that it will enhance the severity of the step change due to the positive feedback between CCN removal and precipitation rate (runaway precipitation, B13). It may also shift the  $N_d$  value at which it occurs to a higher value since small amounts of precipitation at higher  $N_d$  are likely to be amplified by CCN removal. Therefore, we expect open-cell regions to be more likely to occur with aerosol processing in operation.

## 4.3 What is the relative importance of macrophysical and cloud albedo changes for aerosol-induced radiative effects?

Since the impact on  $SW_{\text{upTOA}}$  of stratocumulus is perhaps the primary consideration, it is useful to break down the aerosol-induced changes in this quantity into separate responses due to changes in  $N_d$  (the cloud-albedo effect) and changes in macrophysical cloud properties such as  $LWP_{\text{ic}}$  and  $f_c$ . A method for doing this using an analytical calculation of  $SW_{\text{upTOA}}$  with the time- and domain-mean model cloud property values as inputs is described in Appendix C. Figure 16 shows the results, where the runs shown in Fig. 15 have been compared to the runs with the next highest aerosol concentration. The closeness of the red bars (changes in  $SW_{\text{upTOA}}$  between runs from the online radiation code) to the totals from the value estimates using the analytical formulae suggest that the method works reasonably well.

The results indicate that the cloud-albedo effect (i.e. the change due to  $N_d$  alone with  $LWP_{\text{ic}}$  and  $f_c$  held constant) plays a large role in causing the changes in  $SW_{\text{upTOA}}$  seen between the different runs, causing 44.5, 69.9, and 94.7 % of the total of the absolute changes (see Eq. C7) for the three comparisons made in Fig. 16. The contribution from  $N_d$  changes is largest for the comparison between the two highest  $N_d$  runs since there is very little change in either  $LWP_{\text{ic}}$  or  $f_c$  for those runs. As  $N_d$  is reduced, the contribution from changes in  $LWP_{\text{ic}}$  and  $f_c$  increases, but the comparison between the two lowest- $N_d$  runs indicates that the change due to  $N_d$  is still the single largest factor. However, given that changes to  $LWP_{\text{ic}}$  and  $f_c$  can both be considered macrophysical cloud responses and that there is some ambiguity in the definition of  $LWP_{\text{ic}}$  and  $f_c$  since it depends on the threshold chosen, their changes could be combined into one macrophysical response value. In that case, the percentage

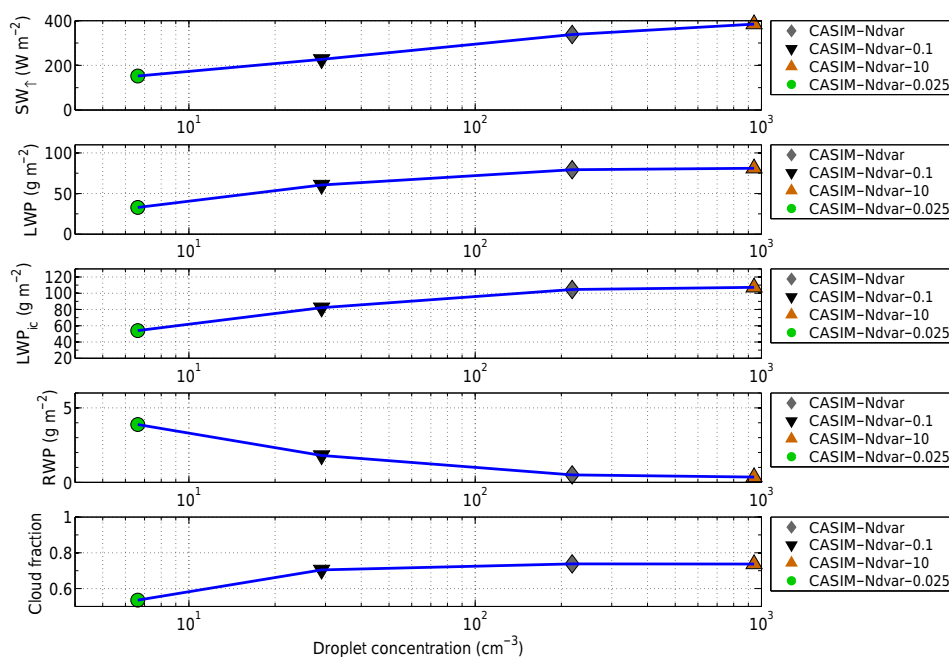


**Figure 15.** Summary plots of domain- and time-mean quantities for the different model runs. The time average is weighted by the incoming SW TOA flux time series to give extra weighting to times when the cloud properties contribute to the SW flux, i.e. mainly in the daytime. The x axis shows droplet concentrations, which are calculated in the same way as for Fig. 3. The top plot shows SW TOA flux, which is followed by LWP (domain mean), in-cloud LWP ( $LWP_{ic}$ ), RWP, and cloud fraction. Cloud fraction is calculated as for Fig. 10. Model data at 30 min intervals between the times of 06:00 UTC (01:12 LST) on 12 November and 00:00 UTC (19:12 LST) on 14 November are used, with the first 6 h of model data being avoided due to spin-up.

change due to this combined macrophysical response would be 55.4 %, compared to 44.6 % for the cloud-albedo ( $N_d$ ) effect, for the comparison between CASIM-Ndvar-0.025 and CASIM-Ndvar-0.1 suggesting that overall macrophysical responses are at least of equal importance when  $N_d$  is low.

#### 4.4 What is the relative importance of the sub-grid cloud scheme?

For these simulations we introduced a sub-grid cloud scheme, which was shown in Fig. 4 to have a significant effect on cloud properties, even at the 1 km  $\Delta x$  value used here. Domain mean LWP values with the cloud scheme switched off were lower than those of the CASIM-Ndvar-0.025 case (lowest-aerosol run) for the first half of the simulation. They were higher for the second half, but were still lower than for the CASIM-Ndvar-0.1 case. Thus, the effect of the cloud scheme was comparable to that of large changes in the aerosol, which means that the inclusion of such a scheme within the UM is vital for the simulation of realistic marine stratocumulus clouds and therefore also for their response to aerosol. This may also be the case for other models at this resolution. Given the importance of the cloud scheme, it would be prudent to perform further investigation in future studies into the setting of the  $RH_{crit}$  parameter (see Ap-

pendix A), or methods for deriving  $RH_{crit}$  that use, for example, sub-grid turbulent kinetic energy.

#### 4.5 Model resolution considerations

The credible simulation of closed-cell stratocumulus using a horizontal resolution ( $\Delta x$ ) of 1 km and a fairly coarse vertical resolution is consistent with previous results in the literature, for example BA12. Close matches to observations have also been reported, using even coarser resolutions of 9 km (Yang et al., 2011) and 14 km (George et al., 2013) with the WRF-Chem model, albeit with the representation of stratocumulus relying heavily on the boundary layer–stratocumulus parameterizations employed.

However, it is likely that a  $\Delta x$  of 1 km or greater will not fully resolve some important effects, especially for cases that involve smaller-scale eddies such as open-cell cases where aerosol removal and cold pool dynamics associated with narrow precipitating regions become more important. Model resolution also affects the spectra of vertical velocities that are represented, which has been shown to have an impact on the number of aerosol particles that are activated into droplets (e.g. Malavelle et al., 2014), and it also has dynamical implications.

Despite this, we note that LES simulations looking at such aspects have been successfully performed, with little sensi-

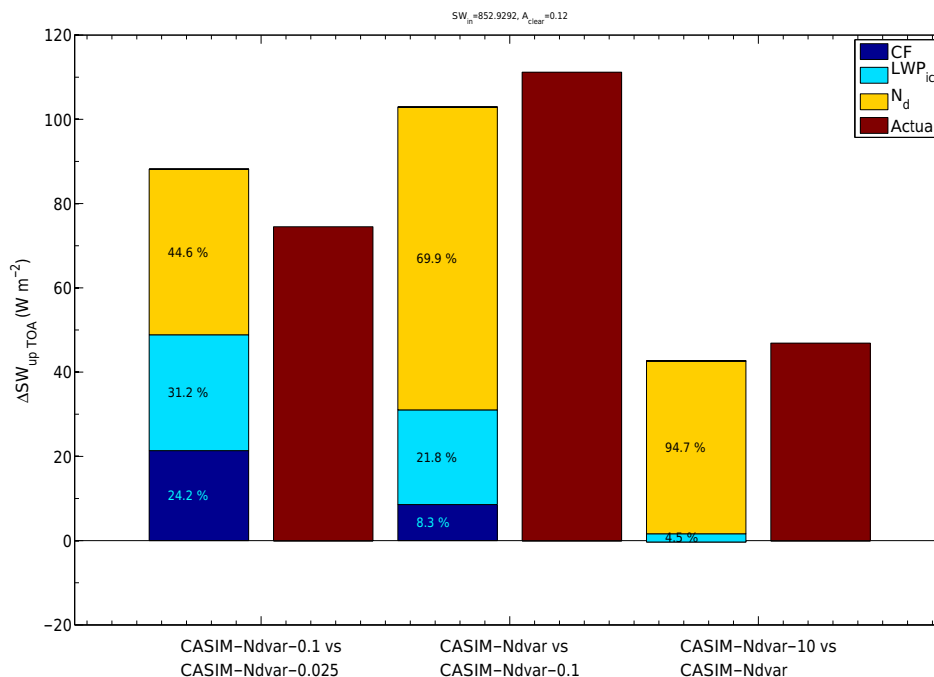


**Figure 16.** Estimated individual contributions to changes in the shortwave upwelling TOA radiation flux ( $\Delta SW_{up,TOA}$ ) due to changes in the domain- and time-mean (weighted as for Fig. 15) cloud properties (cloud fraction,  $f_c$ , in-cloud LWP,  $LWP_{ic}$ , and droplet number concentration,  $N_d$ ; see the legend for the colour labelling) using an analytical formula for scene albedo. Changes in  $SW_{up,TOA}$  are estimated between a given run in Fig. 15 (Run<sub>*i*</sub>) and the run with the next highest aerosol concentration (Run<sub>*i+1*</sub>) by replacing one cloud property of Run<sub>*i*</sub> with that from Run<sub>*i+1*</sub>, i.e. for the  $f_c$  response,  $\Delta SW_{f_c} = SW(f_{c_{i+1}}, LWP_{ic_i}, N_{d_i}) - SW(f_{c_i}, LWP_{ic_i}, N_{d_i})$ , with the compared runs indicated by the  $x$ -axis labels. The percentage that each cloud property contributes to the sum of the absolute changes is shown in the individual bars, e.g. the cloud fraction percentages are given by  $100 \times \Delta SW_{f_c} / (|\Delta SW_{f_c}| + |\Delta SW_{LWP_{ic}}| + |\Delta SW_{N_d}|)$ . The red bars show the actual change in SW from the model output.

tivity to using a higher resolution, when using  $\Delta x$  values of 200 m (Feingold et al., 2015), which is reasonably close to the 1 km resolution used here. Indeed, we do observe some features that resemble open-cells in our simulation (see Sect. 3.2.3), indicating that they start to be resolved using  $\Delta x = 1$  km. A factor to bear in mind here is that the different dynamical solvers used by different models may lead to a varying effective resolution for a given actual grid size. More work is required in order to clarify these issues. In the future we will investigate the model performance for an open-cell or POC case at a range of model resolutions (with aerosol processing included).

As discussed above, our fairly coarse vertical resolution is not adequate to explicitly simulate the entrainment process; previous studies have shown (Stevens and Bretherton, 1999) that a vertical resolution of around 5 m is needed to do this. Therefore, our simulations will rely upon the boundary layer scheme to represent this process. Further work is needed to investigate how well this scheme works and how it interacts with aerosol loading and droplet sizes, whether it is feasible to run over large domains with a very-high-resolution vertical grid near cloud top, and if so, how it affects model perfor-

mance. Issues regarding the ratio of horizontal and vertical grid sizes are also likely to require further attention.

## 5 Conclusions

Stratocumulus clouds are very important for the earth's radiative budget. Aerosols form an integral part of the stratocumulus system and aerosol perturbations can significantly alter the radiative properties of these clouds. Thus, the realistic simulation of stratocumulus and its interaction with aerosol is vital for weather and climate predictions. In this paper we have addressed the question of whether the UM regional model with a new microphysics scheme and a newly coupled sub-grid cloud scheme can produce such a realistic representation of closed-cell stratocumulus and its response to aerosol when employing relatively coarse horizontal and vertical resolutions (1 km and 100 m at the inversion respectively).

We compared UM runs with the recent CASIM microphysics scheme, along with a newly implemented sub-grid cloud scheme against a range of observational metrics. The run with control aerosol concentrations captured the shape of the domain-mean LWP diurnal cycle as observed by satellite

microwave instruments and agreed quantitatively for most of the diurnal cycle, being within around  $10 \text{ g m}^{-2}$  ( $\sim 10\%$ ) at the nighttime maxima. However, an overestimate of  $20\text{--}30 \text{ g m}^{-2}$  ( $\sim 50\text{--}75\%$ ) was observed for the time of the daytime minima, which we suggest is due to a lack of spatial heterogeneity in the imposed model aerosol field, leading to too many cloud droplets offshore and causing a lack of precipitation and hence a lack of LWP removal in those regions. This issue was highlighted by PDFs of model cloud droplet concentrations ( $N_d$ ) that showed a high- $N_d$  mode in agreement with the observations (for the near-shore region), but a lack of the low- $N_d$  mode that was observed in the offshore region.

Daytime cloud fraction distributions from the model matched those from the GOES-10 satellite very closely for the control and high-aerosol cases, especially for cloud fraction values  $> \sim 0.5$ . For these runs, the domain mean cloud fraction during the night also matched that observed to within 3%. PDFs of shortwave TOA fluxes from the control model were very close to those from CERES, except for a slight underestimate in the frequency of values between around  $500$  and  $700 \text{ W m}^{-2}$ . Analysis suggested that this was due to near-shore aerosol concentrations that were too low for the particular times of the CERES overpasses.

Radar observations showed that the modelled and observed cloud depths were quite similar (agreement within  $\sim 18\%$ ), as were the maximum reflectivities attained ( $-1.9 \text{ dBZ}$  in the model vs.  $-5.2 \text{ dBZ}$  in the observations), the latter suggesting that the maximum droplet and raindrop embryo sizes reached in the model were close to those in reality. Model reflectivities also increased with height in a similar manner to the observations in the lower portion of the clouds. However, there were too many low reflectivity values in the model and the height of the modelled boundary layer was too low. The latter is a problem that was likely inherited from the driving global model, which indicates meteorology problems and/or a lack of entrainment in the global model and possibly in the nested model too. The maximum reflectivity was observed to decrease with height towards the cloud top, which was not the case for the models. Possible causes for this model bias may be a lack of entrainment, issues related to the incorrect model boundary layer height, or microphysical issues regarding rain formation.

Our model simulated a monotonic increase in the domain- and time-mean shortwave TOA flux ( $\text{SW}_{\text{upTOA}}$ ) with increasing aerosol concentrations, with values more than doubling between the lowest and highest aerosol cases, reinforcing that aerosol impacts are likely to drastically change the radiative properties of stratocumulus clouds. When aerosol was increased between the two runs with the lowest aerosol concentrations, the aerosol change caused both a large cloud fraction increase and a large in-cloud LWP (cloudy sky only) increase, which was responsible for around half of the observed increase in  $\text{SW}_{\text{upTOA}}$ . Thus, the cloud macrophysical response was very important for this aerosol range. The rest

of the  $\text{SW}_{\text{upTOA}}$  increase was due to the increase in cloud albedo (i.e. droplet number concentration,  $N_d$ , alone). Further increases in aerosol caused only very small cloud fraction increases, suggesting that the cloud fraction response occurs over a fairly narrow range of aerosol concentrations and that traditional aerosol–cloud interaction metrics may not be entirely appropriate for characterizing this.

The in-cloud LWP ( $\text{LWP}_{\text{ic}}$ ) response also diminished with increasing aerosol concentration, such that the  $N_d$  increase (i.e. the cloud-albedo effect) became the dominant effect in terms of causing the observed changes in  $\text{SW}_{\text{upTOA}}$ . In fact the cloud-albedo effect was strong throughout the entire range of aerosol concentrations that were tested, showing that, whilst this process is arguably more simple than the cloud macrophysical response, it is still important to simulate it correctly. Furthermore, for stratocumulus clouds it likely dominates over a wider range of aerosol concentrations than macrophysical responses. Nevertheless, the large macrophysical response of a reduction of cloud fraction and LWP at low aerosol concentrations may be very important in more pristine regions such as offshore from the SE Pacific coastal (VOCALS campaign) region or in the Southern Ocean, for example. Large sensitivities of cloud radiative effects to aerosol may be expected within this low-aerosol regime due to the cloud macrophysical response.

This study suggests that it may be necessary to employ a sub-grid cloud scheme within the UM model for stratocumulus, even at  $1 \text{ km}$  horizontal resolution. This finding may also apply to other models. Without the cloud scheme, mean LWP values were up to around 50% too small, which is a difference that is comparable to that between the lowest and highest aerosol runs (representing an increase in aerosol by a factor of 400) during the first half of the simulation. It may also be the case that a cloud scheme needs to be considered for other aerosol–cloud interaction regional models in order to simulate realistic stratocumulus macrophysical properties.

The use of lower resolution paves the way for larger-area, longer-timescale simulations than have been previously possible with very-high-resolution LES models, or it may even allow global simulations. Domain size could be important to allow the representation of large meteorological features and dynamical feedbacks between large area features such as between open-cell and non-open-cell regions, as well as for examining the wider-scale dynamical impact of cloud–aerosol interactions. Thus, the realistic meteorology of our model represents an important advantage over LES models, which are generally run over smaller domains and employ idealized set-ups that do not allow spatially inhomogeneous meteorological forcing (although there are noted exceptions to the latter limitation: e.g. Chow et al., 2006; Xue et al., 2014, 2016). Since the likelihood is that meteorology has an important influence on stratocumulus and its albedo and that correlations exist between aerosol and meteorology, then the correct representation of meteorology is likely vital when considering cloud–aerosol interactions in a realistic setting.

Once the planned coupling with a detailed aerosol emission, transport, and chemistry model has taken place, correlations between meteorology and aerosol and their impact on cloud properties can be examined.

It is envisioned that the model described here will facilitate the development of sub-grid parameterizations for the aerosol–cloud interaction processes described above for the global model. The use of a nested high-resolution model embedded within an operational model framework, such as is employed here, will allow straightforward testing of the parameterizations against observations since the global and nested models share the same meteorology.

*Data availability.* Raw model data are kept on tape archive available through the JASMIN (<http://www.jasmin.ac.uk/>) service. Please see <http://www.ceda.ac.uk/blog/access-to-the-met-office-mass-archive-on-jasmin-goes-live/> for details on how to arrange access to Met Office data via JASMIN.

## Appendix A: Sub-grid cloud scheme

The sub-grid cloud scheme is based on the scheme described in Smith (1990, hereafter S90). We present only an outline for brevity and refer the reader to S90 for details. The basic assumption is that sub-grid fluctuations in liquid temperature ( $T_L$ ) and/or total water mass mixing ratio ( $q_T$ ) about the grid-box average can give rise to a sub-grid contribution to the total condensed liquid water mass mixing ratio ( $q_{L\text{tot}}$ ) and cloud fraction ( $f_c$ ) within a model grid box.  $T_L$  and  $q_T$  are defined as

$$T_L = T - \frac{L_c}{c_p} q_L, \quad (\text{A1})$$

$$q_T = q_v + q_L, \quad (\text{A2})$$

where (for a given sub-grid element)  $q_v$  and  $q_L$  are the vapour and liquid mass mixing ratios,  $T$  is the temperature,  $L_c$  is the latent heat of condensation, and  $c_p$  is the specific heat capacity of air at constant pressure. Note that  $T_L$  and  $q_T$  are conserved variables during the condensation process. Each given element of the sub-grid distribution has a liquid water content given by

$$q_L = \begin{cases} 0, & s \leq -Q_c \\ Q_c + s, & s > -Q_c, \end{cases} \quad (\text{A3})$$

where  $Q_c$  is the contribution to the liquid water mixing ratio from the grid-box mean quantities and  $s$  represents the contributions due to perturbations about the grid-box mean state. The condition of  $q_L = 0$  for  $s \leq -Q_c$  prevents  $q_L < 0$ .  $Q_c$  is given by

$$\begin{aligned} Q_c &= a_L(\overline{q_T} - q_{\text{sat}}(\overline{T_L}, \overline{p})) \\ &= a_L q_{\text{sat}}(\overline{T_L}, \overline{p})(\overline{\text{RH}}_{\text{tot}} - 1). \end{aligned} \quad (\text{A4})$$

Here,  $q_{\text{sat}}$  refers to the saturation mixing ratio for liquid,  $a_L = \frac{1}{1 + L_c \alpha_L / c_p}$  and  $\alpha_L = \frac{\partial q_{\text{sat}}}{\partial T} |_{T=T_L} \approx \frac{\epsilon L_c q_{\text{sat}}(T_L, P)}{R T_L^2}$ ,  $\overline{\text{RH}}_{\text{tot}} = \overline{q_T} / q_{\text{sat}}(\overline{T_L}, \overline{p})$ , and over bars denote grid-box mean quantities. Note that  $Q_c$  is negative for sub-saturated conditions (in terms of  $q_T$ , i.e.  $\overline{\text{RH}}_{\text{tot}} < 1$ ).

$s$  is given by (Eq. 2.20 of S90)

$$s = a_L(q'_T - \alpha_L T'_L), \quad (\text{A5})$$

where  $q'_T$  and  $T'_L$  are the perturbations of the total water content and liquid temperature of the sub-grid element from the grid-box mean. The sub-grid distribution of  $s$  is specified as an assumed probability density function (PDF) denoted as  $G(s)$ . Note, that this formulation means that the PDFs of  $q_T$  and  $T_L$  do not need to be specified directly, just the PDF of  $s$ . For simplicity, this is assumed to be a triangular-shaped function that is symmetric about  $s = 0$ , where  $s = 0$  represents no perturbation from the mean and is therefore the mean state. The half-width is specified as  $b_s$ . Figure A1 depicts

$G(s)$ . Normalization of  $G(s)$ , i.e.  $\int_{-b_s}^{b_s} G(s) ds = 1$ , dictates that  $G(0) = 1/b_s$ , from which it follows that

$$G(s) = \begin{cases} 0, & s \leq -b_s \\ \frac{b_s + s}{b_s^2}, & -b_s \leq s < 0 \\ \frac{b_s - s}{b_s^2}, & 0 \leq s < b_s \\ 0, & s > b_s \end{cases}. \quad (\text{A6})$$

This sub-grid distribution of  $G(s)$  is assumed to exist in all grid boxes. However, cloud will only be formed for the part of the distribution where  $Q_c + s > 0$  (Eq. A3). Thus, the cloudy part of the sub-grid distribution will lie between  $s = -Q_c$  and  $s = b_s$  such that the cloud fraction ( $f_c$ ) is given by

$$f_c = \int_{-Q_c}^{b_s} G(s) ds. \quad (\text{A7})$$

Therefore, for there to be cloud requires that  $Q_c > -b_s$ . Fig. A1 depicts the transition from a non-cloudy to a cloudy state as  $\text{RH}_{\text{tot}}$  increases. In a highly sub-saturated mean state (in terms of total water, i.e.  $\overline{\text{RH}}_{\text{tot}} \ll 1$ ),  $Q_c$  will be a large negative number such that the start of the integral above will be a large positive number and will lie outside the maximum value in the  $s$  distribution ( $b_s$ ). As  $Q_c$  increases,  $-Q_c$  will decrease until it lies within the  $s$  distribution. The cloud fraction will then be evaluated for the right-hand portion of the  $G(s)$  distribution (the shaded part depicted in Fig. A1).  $\overline{\text{RH}}_{\text{tot}}$  at the point at which  $-Q_c = b_s$  (i.e. where cloud begins to form) is denoted as the critical total relative humidity  $\text{RH}_{\text{crit}}$ . Thus, from Eq. (A4) and the definition of  $\overline{\text{RH}}_{\text{tot}}$  we can write

$$\begin{aligned} b_s &= -a_L(\overline{q_T} - q_{\text{sat}}(\overline{T_L}, \overline{p})) \\ &= a_L q_{\text{sat}}(\overline{T_L}, \overline{p})(1 - \overline{\text{RH}}_{\text{crit}}), \end{aligned} \quad (\text{A8})$$

so that  $b_s$  can also be specified in terms of  $\overline{\text{RH}}_{\text{crit}}$ ,  $\overline{T_L}$ , and  $\overline{p}$ . We use the same  $\text{RH}_{\text{crit}}$  values as used for the UM operational model, which are given in Table A1.

The solution for  $f_c$  is (by combining Eqs. A6 and A7)

$$f_c = \begin{cases} 0, & Q_N \leq -1 \\ \frac{1}{2}(1 + Q_N)^2, & -1 < Q_N \leq 0 \\ 1 - \frac{1}{2}(1 - Q_N)^2, & 0 < Q_N \leq 1 \\ 1, & 1 \leq Q_N \end{cases}, \quad (\text{A9})$$

where we define  $Q_N = Q_c/b_s$ .  $Q_N$  can be written as a function of  $\overline{\text{RH}}_{\text{tot}}$  and  $\text{RH}_{\text{crit}}$  as follows (using Eqs. A4 and A8):

$$Q_N = \frac{Q_c}{b_s} = \frac{a_L(\overline{q_T} - q_{\text{sat}}(\overline{T_L}, \overline{p}))}{a_L q_{\text{sat}}(\overline{T_L}, \overline{p})(1 - \overline{\text{RH}}_{\text{crit}})} = \frac{\overline{\text{RH}}_{\text{tot}} - 1}{1 - \overline{\text{RH}}_{\text{crit}}}, \quad (\text{A10})$$

which are both constant during the cloud formation process, and so  $f_c$  can be calculated directly from the a priori grid-box mean values.

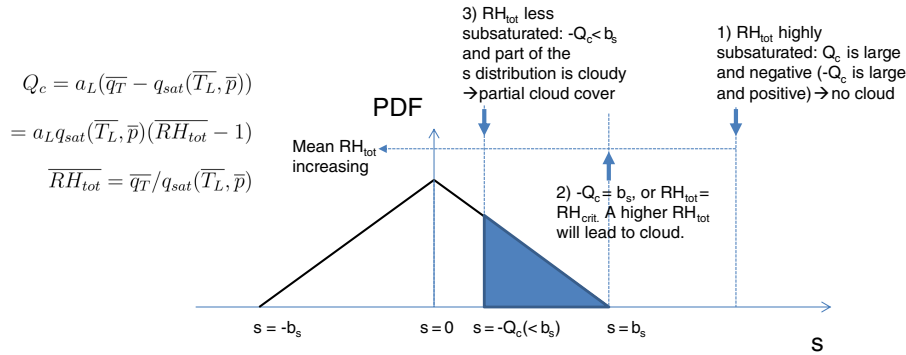


**Figure A1.** The assumed triangular-shaped PDF,  $G(s)$ , to represent the sub-grid distribution of  $s$  (Eq. A6), which is the liquid water mass mixing ratio associated with perturbations about the mean grid-box state (for which  $s = 0$ ). The half-width of the distribution is called  $b_s$  and is a specified parameter. Cloud forms for the part of the distribution for which  $q_L > 0$ , which corresponds to  $s > -Q_c$  (Eq. A3) if  $-Q_c < b_s$ , with the cloud fraction given by  $\int_{-Q_c}^{b_s} G(s) ds$  (shaded part of the figure; note that the shading applies to situation (3) as labelled in the figure, i.e.  $-Q_c < b_s$ ).  $Q_c$  is the amount of total water content above saturation for the grid-box mean state and thus increases as the grid-box mean total water relative humidity ( $\overline{RH}_{tot}$ ) increases. For highly sub-saturated mean conditions (in terms of  $\overline{RH}_{tot}$ ),  $Q_c$  is large and negative such that  $-Q_c > b_s$  and no part of the sub-grid distribution is cloudy (see (1) in the figure). With increasing  $\overline{RH}_{tot}$ , a critical relative humidity (denoted as  $RH_{crit}$ ) is reached (2), where  $-Q_c = b_s$ . Further increases in  $\overline{RH}_{tot}$  will lead to partial cloud coverage (e.g. (3)) with full cloud cover only being reached when  $Q_c = b_s$ , corresponding to  $\overline{RH}_{tot} > 1$ .

The mean liquid water mass mixing ratio is calculated as follows:

$$\bar{q}_L = \int_{-Q_c}^{b_s} (Q_c + s)G(s)ds. \quad (\text{A11})$$

The solution to this is

$$\frac{\bar{q}_L}{b_s} = \begin{cases} 0, & Q_N \leq -1 \\ \frac{1}{6}(1 + Q_N)^3, & -1 < Q_N \leq 0 \\ Q_N + \frac{1}{6}(1 - Q_N)^3, & 0 < Q_N \leq 1 \\ Q_N, & 1 \leq Q_N \end{cases}. \quad (\text{A12})$$

Thus, the solution for  $\bar{q}_L$  contains the  $b_s$  term, which is calculated from  $Q_c$  via Eqs. (A4) and (A8). Equation (A4), which defines  $Q_c$ , is based upon a first-order Taylor expansion approximation of  $q_{sat}(T)$  as a function of  $q_{sat}(T_L)$  since the final value of  $T$  is unknown a priori as it is a function of  $q_L$ , which has yet to be determined. Inaccuracy due to this approximation can be improved by an iterative procedure, which is fully described in Wilson (2011).

Advection operates upon the grid-box mean mixing ratio and number concentrations of liquid water (denoted as  $\bar{q}_L$  and  $\bar{n}_L$ ). However, before the calculation of the microphysical process rates,  $\bar{q}_L$  and  $\bar{n}_L$  are divided by  $f_c$  so that the mean values over only the cloudy part of the grid box are used. Once the process rates have been calculated, the ones that change  $\bar{q}_L$  and  $\bar{n}_L$  are multiplied by  $f_c$ . This ensures that any non-linearity in the microphysical processes is captured, i.e. cases where  $f_c \times P(\frac{q_c}{f_c}, \frac{n_c}{f_c}) \neq P(\bar{q}_c, \bar{n}_c)$ , where  $P(q_c, n_c)$  represents a microphysical process rate as a function of  $q_c$

**Table A1.** The  $RH_{crit}$  values used in the sub-grid cloud scheme.

Model level	$RH_{crit}$
1	0.96
2	0.94
3	0.92
4	0.9
5	0.89
6	0.88
7	0.87
8	0.86
9	0.85
10	0.84
11	0.84
12	0.83
13	0.82
14	0.81
$\geq 15$	0.8

and  $n_c$ . The radiation scheme also takes into account  $f_c$  for liquid clouds in a similar manner.

It is also possible to estimate a fraction over which precipitation is likely to be present. For example Chosson et al. (2014) makes such an estimate based on the cloud fraction in the layers above. However, problems may arise due to separation of the precipitating regions from the cloudy regions above by horizontal advection. Thus, for this paper we have assumed a precipitation fraction of 1.0 for simplicity and will test the effect of a sub-grid precipitation fraction in subsequent work. Since we have concentrated on warm clouds here, no account of a sub-grid ice cloud fraction has been made.

## Appendix B: Observation details

The observations used for the model evaluation in this paper are now described. See Table 5 for a summary.

There are several satellites that have microwave radiometer instruments onboard and that provide coverage of the study region. These instruments include AMSR-E (onboard Aqua), the SSMI–SSMIS instruments (onboard the f13, f15, f16, and f17 satellites), TMI (onboard TRMM), and Wind-sat (onboard Coriolis). These instruments report an overall average LWP for the cloudy and clear parts of a given region (i.e. no attempt is made to separate cloudy and clear pixels). We use the gridded daily data that are provided at  $0.25^\circ \times 0.25^\circ$  resolution from [www.remss.com](http://www.remss.com) and are separated into daytime and nighttime overpasses. The native resolution for the 37 GHz LWP retrieval that is used for the LWP retrievals varies from instrument to instrument, with the lowest resolution being  $\sim 37 \times 28$  km for the SSMI instruments. Snapshots within the study region are made by the different instruments at various times of the day, allowing a diurnal cycle to be built up from their combination. Further details on the specifics of the retrieval algorithms for each instrument can be found at <http://www.remss.com/missions>.

Microwave radiometers provide a fairly reliable estimate of cloud LWP, although some errors have been identified in the form of non-zero values being reported in clear-sky situations. However, examining AMSR-E data, Lebsock and Su (2014) reported that these errors were larger for situations with high column water vapour values; the mean clear-sky bias in the SE Pacific was only around  $2\text{--}3 \text{ g m}^{-2}$ .

Data from the GOES-10 geostationary satellite are also extensively used in our study. A special data set was created for the VOCALS field campaign that covers the location and period of the simulations performed in this study. The data were analysed as in Minnis et al. (2008) using the methods of Minnis et al. (2011) as described in Wood et al. (2011b) and Allen et al. (2013). We mainly use the retrievals of cloud optical depth ( $\tau$ ) and effective radius ( $r_e$ ) that are provided at 4 km spatial resolution every 30 min. From these two quantities we make an estimate of LWP following Wood and Hartmann (2006):

$$\text{LWP} = 5/9 \rho_w \tau r_e, \quad (\text{B1})$$

where  $\rho_w$  is the density of liquid water.

Estimates of cloud droplet concentrations are also made using the technique described in Grosvenor and Wood (2014, hereafter GW14). We only use the daytime data in this study since the retrieval of  $r_e$  and  $\tau$  when there is no daylight uses an experimental technique for which the reliability is not well proven. In addition, daytime retrievals where the solar zenith angle is larger than  $65^\circ$  are not used due to the likelihood of biases (GW14).

Painemal et al. (2012) performed a comparison of the GOES-10  $r_e$ ,  $\tau$ , and  $N_d$  retrievals to aircraft and MODIS satellite observations for the VOCALS field campaign pe-

riod. Since our simulations are performed during the time of VOCALS and very close to where the aircraft measurements took place, the GOES-10 errors reported should be representative of the errors that we can expect for our study. The GOES-10  $r_e$  was found to be well correlated ( $r = 0.91$ ) with the aircraft values, but biased high by 22 %, which was a very similar positive bias to that reported for MODIS  $r_e$  values. GOES-10  $\tau$  also correlated well with the aircraft observations ( $r = 0.79$ ), but had a much smaller mean bias of only 6 %. LWP estimates using the equation above demonstrated a mean positive bias of 14.7 % (attributable to the positive  $r_e$  bias), an RMSE of  $26.9 \text{ g m}^{-2}$ , and  $r = 0.84$ . The mean bias for  $N_d$  (calculated using the same method that we apply) was  $-20$  %, with  $r = 0.91$  and an RMSE of  $36 \text{ cm}^{-3}$ ; this fairly low bias was achieved despite the strong dependence of  $N_d$  on  $r_e$  ( $N_d \propto r_e^{-2.5}$ ) and the relatively high  $r_e$  bias due to compensating biases in some of the other factors used to estimate  $N_d$ , as described in Painemal and Zuidema (2011).

Long-wave (LW) and shortwave (SW) top-of-the-atmosphere (TOA) radiative fluxes are obtained from the CERES instruments (Wielicki et al., 1996) that are onboard both the Aqua and Terra satellites. We use the SSF Level-2 product (CERES\_SSF\_XTRK-MODIS\_Edition4A, taken from <http://ceres.larc.nasa.gov/products.php?product=SSF-Level2>), which is provided at a nominal resolution of 20 km. These instruments provide snapshots of the radiative fluxes at local times (for the swath centre) of around 01:30 and 13:30 for the Aqua satellite and 10:30 and 22:30 for the Terra satellite, although we note that SW fluxes are only available during daylight hours. Also, CERES data are unavailable for the afternoon overpass on 13 November 2008 (the second day of our simulation period) for the Aqua instrument. Loeb et al. (2007) estimate an uncertainty in CERES fluxes of less than 5 % for SW and less than 3 % for LW for overcast, moderately thick, or thick low clouds over the ocean, which are the predominant cloud type in the region of our study.

The RV *Ronald H. Brown* was stationed near  $20^\circ \text{ S}$ ,  $75^\circ \text{ W}$ , which is near the centre of our model domain. Data were gathered from the onboard instruments throughout the modelled period, which we use to help evaluate the model. A microwave radiometer provided LWP estimates every 10 min (Zuidema et al., 2005; de Szoeke et al., 2012). The 94 GHz (W-band) cloud radar produced data at the same time frequency (Moran et al., 2011; de Szoeke et al., 2012; Fairall et al., 2014) and is used to evaluate model drizzle and large droplet properties.

## Appendix C: Shortwave radiation calculations

The shortwave top-of-the-atmosphere (TOA) upwards radiative flux ( $\text{SW}_{\text{upTOA}}$ ) is estimated from the domain- and time-mean in-cloud LWP ( $\text{LWP}_{\text{ic}}$ ), droplet concentration ( $N_d$ ), and the cloud fraction ( $f_c$ ) using analytical formulae. Firstly,

the cloud optical depth ( $\tau$ ) is estimated by assuming that the clouds are adiabatic (or some constant fraction of adiabatic) so that their liquid water increases linearly with height, and it is assumed that  $N_d$  is constant throughout their depth. Observations suggest that both are valid assumptions for stratocumulus clouds (Albrecht et al., 1990; Zuidema et al., 2005; Painemal and Zuidema, 2011; Miles et al., 2000; Wood, 2005). With these assumptions  $\tau$  can be related to  $LWP_{ic}$  and  $N_d$  by rearranging the formula for  $N_d$  given in GW14 (Eq. A1 of that paper) and replacing the effective radius ( $r_e$ ) using Eq. (B1) to give

$$\tau = \frac{(9/5)^{5/2} \pi k Q^3}{2\sqrt{10} \rho_w^2 c(T, P)^{1/2}} N_d^{1/3} LWP_{ic}^{5/6}$$

$$k = (r_v/r_e)^3, \quad (C1)$$

where  $\tau$  is the cloud optical thickness,  $r_e$  and  $r_v$  are the cloud top effective and volume mean radius respectively,  $k$  is cube of the ratio of  $r_v$  to  $r_e$ ,  $\rho_w$  is the density of water, and  $Q$  is the scattering efficiency.  $Q$  has been shown to have a constant value very close to 2 for droplet radii that are much larger than the wavelength of light concerned (Bennartz, 2007).  $c(T, P)$  is the rate of increase of liquid water content ( $q_L$ ) with height ( $dq_L/dz$ , with units  $\text{kg m}^{-4}$  and is referred to as the condensation rate in Bennartz (2007) or the water content lapse rate in Painemal and Zuidema, 2011). See Ahmad et al. (2013) for a definition. The cloud-top temperature as determined by GOES-10 is used for the temperature ( $T$ ) in the calculation of  $c(T, P)$ , along with a constant pressure ( $P$ ) of 850 hPa. GW14 shows that these two approximations are likely to cause very little error.

The cloud albedo ( $A_c$ ) is then estimated using Eq. (24.38) of Seinfeld and Pandis (2006), which is based on the two-stream approximation for a non-absorbing, horizontally homogeneous cloud:

$$A_c = \frac{\tau}{\tau + 7.7}. \quad (C2)$$

The shortwave upwards flux at cloud top ( $SW_{upCT}$ ) for a given cloud fraction ( $f_c$ ) can then be calculated as

$$SW_{upCT} = SW_{downCT} (f_c A_c + (1 - f_c) A_s), \quad (C3)$$

where  $SW_{downCT}$  is the SW downwelling flux at cloud top and  $A_s$  is the surface albedo.  $SW_{downCT}$  is approximated as the SW downwelling flux at the surface ( $SW_{downSURF}$ ), which is estimated from the model data for clear columns. Thus, this estimate neglects any additional scattering or absorption between the typical cloud-top heights and the surface. However, since the cloud-top heights are low, this should not lead to a large error.  $SW_{upTOA}$  can then be estimated as

$$SW_{upTOA} = T_r SW_{upCT}, \quad (C4)$$

where  $T_r$  is the transmission of the atmosphere, which is assumed constant and is estimated using

$$T_r = SW_{downSURF} / SW_{downTOA}. \quad (C5)$$

Here we are assuming that the downward transmission is equal to the upward transmission.

Using these formulae, we calculated  $SW_{upTOA}$  from the model domain- and time-mean cloud properties. Time means were weighted by  $SW_{downTOA}$  in order to prioritize the day-time values. However, when weighted equally over all times, the relationships between the different model runs (i.e. different  $N_d$  values) were very similar, although the magnitudes of the averages were changed. We found that the analytical estimates were within 13 % of the actual mean  $SW_{upTOA}$  as calculated online by the model radiation code for the four model runs shown in Fig. 15. The analytical formulae were then used to estimate the individual effects on  $SW_{upTOA}$  of the changes in  $f_c$ ,  $LWP_{ic}$ , and  $N_d$  between the different runs, with each run having different prescribed aerosol loadings. Changes in  $SW_{upTOA}$  are estimated between a given run in Fig. 15 ( $Run_i$ ) and the run with the next highest aerosol concentration ( $Run_{i+1}$ ) by replacing one cloud property of  $Run_i$  with that from  $Run_{i+1}$ , e.g. for the cloud fraction response,

$$\Delta SW_{f_c} = SW(f_{c_{i+1}}, LWP_{ic_i}, N_{d_i}) - SW(f_{c_i}, LWP_{ic_i}, N_{d_i}). \quad (C6)$$

The percentage that each cloud property contributes to the sum of the absolute changes ( $P_x$ ) for a given  $Run_i$  is also calculated (as shown as text in the individual bars in Fig. 16), e.g. for cloud fraction:

$$P_{f_c} = \frac{100 \times \Delta SW_{f_c}}{|\Delta SW_{f_c}| + |\Delta SW_{LWP_{ic}}| + |\Delta SW_{N_d}|}. \quad (C7)$$

*Author contributions.* D. P. Grosvenor, P. R. Field, and A. A. Hill developed the concepts and ideas for the direction of the paper. B. S. Shipway wrote the CASIM microphysics code. D. P. Grosvenor, A. A. Hill, and P. R. Field helped to further develop the CASIM microphysics code and performed the coupling of the sub-grid cloud scheme parameterization. D. P. Grosvenor, P. R. Field, and A. A. Hill helped set up and complete the model runs. D. P. Grosvenor performed the model data analysis, compiled and analysed the observational data sets, and wrote the majority of the manuscript, along with input and comments by P. R. Field, A. A. Hill, and B. S. Shipway.

*Competing interests.* The authors declare that they have no conflict of interest.

*Acknowledgements.* This work was funded by both the University of Leeds and the NERC CLARIFY grant number NE/L013479/1. We acknowledge use of the MONSooN system, a collaborative facility supplied under the Joint Weather and Climate Research Programme, a strategic partnership between the Met Office and the Natural Environment Research Council. The GOES-10 and the RV *Ronald H. Brown* radiometer and radar data data sets were originally provided by NCAR/EOL under sponsorship of the National Science Foundation NCAR/EOL and are available at <http://data.eol.ucar.edu/NCAR/EOL>. We thank Steve Abel and Ian Boutle for the assimilation and provision of those radiometer and radar data sets and we thank Grant Allen for the assimilation and provision of the GOES-10 data set. Peter Minnett is acknowledged for the use of his microwave radiometer onboard the RV *Ronald H. Brown* during the VOCALS field campaign. AMSR-E, SSMI/SSMIS, Windsat, and TMI data are produced by Remote Sensing Systems and sponsored by the NASA Earth Science MEaSUREs DISCOVER Project and the NASA AMSR-E Science Team. Data are available at [www.remss.com](http://www.remss.com). We thank Stuart Webster for his help setting up the nested suite of simulations. Finally, we thank the two anonymous referees who helped to improve the paper through their constructive comments.

Edited by: T. Takemura

Reviewed by: two anonymous referees

## References

- Abdul-Razzak, H. and Ghan, S. J.: A parameterization of aerosol activation: 2. Multiple aerosol types, *J. Geophys. Res.*, 105, 6837, doi:10.1029/1999jd901161, 2000.
- Abel, S. J., Walters, D. N., and Allen, G.: Evaluation of stratocumulus cloud prediction in the Met Office forecast model during VOCALS-REx, *Atmos. Chem. Phys.*, 10, 10541–10559, doi:10.5194/acp-10-10541-2010, 2010.
- Ackerman, A. S., Toon, O. B., Taylor, J. P., Johnson, D. W., Hobbs, P. V., and Ferek, R. J.: Effects of Aerosols on Cloud Albedo: Evaluation of Twomey's Parameterization of Cloud Susceptibility Using Measurements of Ship Tracks, *J. Atmos. Sci.*, 57, 2684–2695, doi:10.1175/1520-0469(2000)057<2684:eoaca>2.0.co;2, 2000.
- Ackerman, A. S., Kirkpatrick, M. P., Stevens, D. E., and Toon, O. B.: The impact of humidity above stratiform clouds on indirect aerosol climate forcing, *Nature*, 432, 1014–1017, doi:10.1038/nature03174, 2004.
- Ahmad, I., Mielonen, T., Grosvenor, D. P., Portin, H. J., Arola, A., Mikkonen, S., Kühn, T., Leskinen, A., Joutsensaari, J., Kompula, M., Lehtinen, K. E. J., Laaksonen, A., and Romakkaniemi, S.: Long-term measurements of cloud droplet concentrations and aerosol–cloud interactions in continental boundary layer clouds, *Tellus B*, 65, 20138, doi:10.3402/tellusb.v65i0.20138, 2013.
- Albrecht, B., Fairall, C., Thomson, D., White, A., Snider, J., and Schubert, W.: Surface-Based Remote-Sensing Of The Observed And The Adiabatic Liquid Water-Content Of Stratocumulus Clouds, *Geophys. Res. Lett.*, 17, 89–92, doi:10.1029/G1017i001p00089, 1990.
- Albrecht, B. A.: Aerosols, Cloud Microphysics, and Fractional Cloudiness, *Science*, 245, 1227–1230, 1989.
- Allen, G., Vaughan, G., Toniazzo, T., Coe, H., Connolly, P., Yuter, S. E., Burleyson, C. D., Minnis, P., and Ayers, J. K.: Gravity-wave-induced perturbations in marine stratocumulus, *Q. J. Roy. Meteor. Soc.*, 139, 32–45, doi:10.1002/qj.1952, 2013.
- Beheng, K.: A parameterization of warm cloud microphysical conversion processes, *Atmos. Res.*, 33, 193–206, doi:10.1016/0169-8095(94)90020-5, 1994.
- Bennartz, R.: Global assessment of marine boundary layer cloud droplet number concentration from satellite, *J. Geophys. Res.-Atmos.*, 112, D02201, doi:10.1029/2006JD007547, 2007.
- Berner, A. H., Bretherton, C. S., Wood, R., and Muhlbauer, A.: Marine boundary layer cloud regimes and POC formation in a CRM coupled to a bulk aerosol scheme, *Atmos. Chem. Phys.*, 13, 12549–12572, doi:10.5194/acp-13-12549-2013, 2013.
- Bony, S.: Marine boundary layer clouds at the heart of tropical cloud feedback uncertainties in climate models, *Geophys. Res. Lett.*, 32, L20806, doi:10.1029/2005gl023851, 2005.
- Boutle, I. A. and Abel, S. J.: Microphysical controls on the stratocumulus topped boundary-layer structure during VOCALS-REx, *Atmos. Chem. Phys.*, 12, 2849–2863, doi:10.5194/acp-12-2849-2012, 2012.
- Bretherton, C. S., Blossey, P. N., and Uchida, J.: Cloud droplet sedimentation, entrainment efficiency, and subtropical stratocumulus albedo, *Geophys. Res. Lett.*, 34, L03813, doi:10.1029/2006GL027648, 2007.
- Chosson, F., Vaillancourt, P. A., Milbrandt, J. A., Yau, M. K., and Zadra, A.: Adapting Two-Moment Microphysics Schemes across Model Resolutions: Subgrid Cloud and Precipitation Fraction and Microphysical Sub-Time Step, *J. Atmos. Sci.*, 71, 2635–2653, doi:10.1175/jas-d-13-0367.1, 2014.
- Chow, F. K., Weigel, A. P., Street, R. L., Rotach, M. W., and Xue, M.: High-Resolution Large-Eddy Simulations of Flow in a Steep Alpine Valley. Part I: Methodology, Verification, and Sensitivity Experiments, *J. Appl. Meteorol. Clim.*, 45, 63–86, doi:10.1175/jam2322.1, 2006.
- Coakley, J. A. and Walsh, C. D.: Limits to the Aerosol Indirect Radiative Effect Derived from Observations of Ship Tracks, *J. Atmos. Sci.*, 59, 668–680, doi:10.1175/1520-0469(2002)059<0668:ltair>2.0.co;2, 2002.
- de Szoeke, S. P., Yuter, S., Mechem, D., Fairall, C. W., Burleyson, C. D., and Zuidema, P.: Observations of Stratocumulus Clouds and Their Effect on the Eastern Pacific Surface Heat Budget

- along 20°S, *J. Climate*, 25, 8542–8567, doi:10.1175/jcli-d-11-00618.1, 2012.
- Fairall, C. W., Pezoa, S., Moran, K., and Wolfe, D.: An observation of sea-spray microphysics by airborne Doppler radar, *Geophys. Res. Lett.*, 41, 3658–3665, doi:10.1002/2014gl060062, 2014.
- Feingold, G. and Kreidenweis, S. M.: Cloud processing of aerosol as modeled by a large eddy simulation with coupled microphysics and aqueous chemistry, *J. Geophys. Res.-Atmos.*, 107, AAC 6–1–AAC 6–15, doi:10.1029/2002jd002054, 2002.
- Feingold, G., Koren, I., Yamaguchi, T., and Kazil, J.: On the reversibility of transitions between closed and open cellular convection, *Atmos. Chem. Phys.*, 15, 7351–7367, doi:10.5194/acp-15-7351-2015, 2015.
- George, R. C., Wood, R., Bretherton, C. S., and Painter, G.: Development and impact of hooks of high droplet concentration on remote southeast Pacific stratocumulus, *Atmos. Chem. Phys.*, 13, 6305–6328, doi:10.5194/acp-13-6305-2013, 2013.
- Grosvenor, D. P. and Wood, R.: The effect of solar zenith angle on MODIS cloud optical and microphysical retrievals within marine liquid water clouds, *Atmos. Chem. Phys.*, 14, 7291–7321, doi:10.5194/acp-14-7291-2014, 2014.
- Hartmann, D. L., Ockert-Bell, M. E., and Michelsen, M. L.: The Effect of Cloud Type on Earth's Energy Balance: Global Analysis, *J. Climate*, 5, 1281–1304, doi:10.1175/1520-0442(1992)005<1281:teocto>2.0.co;2, 1992.
- Hill, A. A., Feingold, G., and Jiang, H.: The Influence of Entrainment and Mixing Assumption on Aerosol–Cloud Interactions in Marine Stratocumulus, *J. Atmos. Sci.*, 66, 1450–1464, doi:10.1175/2008jas2909.1, 2009.
- Hill, A. A., Shipway, B. J., and Boutle, I. A.: How sensitive are aerosol-precipitation interactions to the warm rain representation?, *J. Adv. Model. Earth Syst.*, 7, 987–1004, doi:10.1002/2014ms000422, 2015.
- Khairoutdinov, M. and Kogan, Y.: A New Cloud Physics Parameterization in a Large-Eddy Simulation Model of Marine Stratocumulus, *Mon. Weather Rev.*, 128, 229–243, doi:10.1175/1520-0493(2000)128<0229:ANCPPI>2.0.CO;2, 2000.
- Koike, M., Takegawa, N., Moteki, N., Kondo, Y., Nakamura, H., Kita, K., Matsui, H., Oshima, N., Kajino, M., and Nakajima, T. Y.: Measurements of regional-scale aerosol impacts on cloud microphysics over the East China Sea: Possible influences of warm sea surface temperature over the Kuroshio ocean current, *J. Geophys. Res.-Atmos.*, 117, D17205, doi:10.1029/2011jd017324, 2012.
- Latham, J., Rasch, P., Chen, C.-C., Kettles, L., Gadian, A., Gettelman, A., Morrison, H., Bower, K., and Choullarton, T.: Global temperature stabilization via controlled albedo enhancement of low-level maritime clouds, *Philos. T. R. Soc. A*, 366, 3969–3987, doi:10.1098/rsta.2008.0137, 2008.
- Lebsock, M. and Su, H.: Application of active spaceborne remote sensing for understanding biases between passive cloud water path retrievals, *J. Geophys. Res.-Atmos.*, 119, 8962–8979, doi:10.1002/2014jd021568, 2014.
- Lock, A. P., Brown, A. R., Bush, M. R., Martin, G. M., and Smith, R. N. B.: A New Boundary Layer Mixing Scheme. Part I: Scheme Description and Single-Column Model Tests, *Mon. Weather Rev.*, 128, 3187–3199, doi:10.1175/1520-0493(2000)128<3187:anblms>2.0.co;2, 2000.
- Loeb, N. G., Kato, S., Loukachine, K., Manalo-Smith, N., and Doelling, D. R.: Angular Distribution Models for Top-of-Atmosphere Radiative Flux Estimation from the Clouds and the Earth's Radiant Energy System Instrument on the Terra Satellite. Part II: Validation, *J. Atmos. Ocean. Tech.*, 24, 564–584, doi:10.1175/jtech1983.1, 2007.
- Malavelle, F. F., Haywood, J. M., Field, P. R., Hill, A. A., Abel, S. J., Lock, A. P., Shipway, B. J., and McBeath, K.: A method to represent subgrid-scale updraft velocity in kilometer-scale models: Implication for aerosol activation, *J. Geophys. Res.-Atmos.*, 119, 4149–4173, doi:10.1002/2013jd021218, 2014.
- Miles, N., Verlinde, J., and Clothiaux, E.: Cloud droplet size distributions in low-level stratiform clouds, *J. Atmos. Sci.*, 57, 295–311, doi:10.1175/1520-0469(2000)057<0295:CDSIL>2.0.CO;2, 2000.
- Miller, N. B., Shupe, M. D., Cox, C. J., Walden, V. P., Turner, D. D., and Steffen, K.: Cloud Radiative Forcing at Summit, Greenland, *J. Climate*, 28, 6267–6280, doi:10.1175/jcli-d-15-0076.1, 015.
- Minnis, P., Nguyen, L., Palikonda, R., Heck, P. W., Spangenberg, D. A., Doelling, D. R., Ayers, J. K., William L. Smith, J., Khaiyer, M. M., Treppe, Q. Z., Avey, L. A., Chang, F.-L., Yost, C. R., Chee, T. L., and Szedung, S.-M.: Near-real time cloud retrievals from operational and research meteorological satellites, in: *Remote Sensing of Clouds and the Atmosphere XIII*, edited by: Picard, R. H., Comeron, A., Schäfer, K., Amodeo, A., and van Weele, M., SPIE-Intl. Soc. Optical. Eng., doi:10.1117/12.800344, 2008.
- Minnis, P., Sun-Mack, S., Young, D. F., Heck, P. W., Garber, D. P., Chen, Y., Spangenberg, D. A., Arduini, R. F., Treppe, Q. Z., Smith, W. L., Ayers, J. K., Gibson, S. C., Miller, W. F., Hong, G., Chakrapani, V., Takano, Y., Liou, K.-N., Xie, Y., and Yang, P.: CERES Edition-2 Cloud Property Retrievals Using TRMM VIRS and Terra and Aqua MODIS Data. Part I: Algorithms, *IEEE Transactions on Geoscience and Remote Sensing*, 49, 4374–4400, doi:10.1109/tgrs.2011.2144601, 2011.
- Moran, K., Pezoa, S., Fairall, C., Williams, C., Ayers, T., Brewer, A., de Zoeke, S. P., and Ghate, V.: A Motion-Stabilized W-Band Radar for Shipboard Observations of Marine Boundary-Layer Clouds, *Bound.-Lay. Meteorol.*, 143, 3–24, doi:10.1007/s10546-011-9674-5, 2011.
- Painemal, D. and Zuidema, P.: Assessment of MODIS cloud effective radius and optical thickness retrievals over the Southeast Pacific with VOCALS-REX in situ measurements, *J. Geophys. Res.-Atmos.*, 116, D24206, doi:10.1029/2011JD016155, 2011.
- Painemal, D., Minnis, P., Ayers, J. K., and O'Neill, L.: GOES-10 microphysical retrievals in marine warm clouds: Multi-instrument validation and daytime cycle over the southeast Pacific, *J. Geophys. Res.-Atmos.*, 117, D19212, doi:10.1029/2012jd017822, 2012.
- Platnick, S., Durkee, P. A., Nielsen, K., Taylor, J. P., Tsay, S.-C., King, M. D., Ferek, R. J., Hobbs, P. V., and Rottman, J. W.: The Role of Background Cloud Microphysics in the Radiative Formation of Ship Tracks, *J. Atmos. Sci.*, 57, 2607–2624, doi:10.1175/1520-0469(2000)057<2607:trobcm>2.0.co;2, 2000.
- Quaas, J., Stevens, B., Stier, P., and Lohmann, U.: Interpreting the cloud cover – aerosol optical depth relationship found in satellite data using a general circulation model, *Atmos. Chem. Phys.*, 10, 6129–6135, doi:10.5194/acp-10-6129-2010, 2010.

- Rosenfeld, D., Kaufman, Y. J., and Koren, I.: Switching cloud cover and dynamical regimes from open to closed Benard cells in response to the suppression of precipitation by aerosols, *Atmos. Chem. Phys.*, 6, 2503–2511, doi:10.5194/acp-6-2503-2006, 2006.
- Saide, P. E., Spak, S. N., Carmichael, G. R., Mena-Carrasco, M. A., Yang, Q., Howell, S., Leon, D. C., Snider, J. R., Bandy, A. R., Collett, J. L., Benedict, K. B., de Szoeko, S. P., Hawkins, L. N., Allen, G., Crawford, I., Crosier, J., and Springston, S. R.: Evaluating WRF-Chem aerosol indirect effects in Southeast Pacific marine stratocumulus during VOCALS-REx, *Atmos. Chem. Phys.*, 12, 3045–3064, doi:10.5194/acp-12-3045-2012, 2012.
- Seinfeld, J. H. and Pandis, S. N.: *Atmospheric chemistry and physics: from air pollution to climate change*, Hoboken, N.J., J. Wiley, 2nd Edn., 2006.
- Shipway, B. J. and Hill, A. A.: Diagnosis of systematic differences between multiple parametrizations of warm rain microphysics using a kinematic framework, *Q. J. Roy. Meteor. Soc.*, 138, 2196–2211, doi:10.1002/qj.1913, 2012.
- Smith, R. N. B.: A scheme for predicting layer clouds and their water content in a general circulation model, *Q. J. Roy. Meteor. Soc.*, 116, 435–460, doi:10.1002/qj.49711649210, 1990.
- Soden, B. J. and Vecchi, G. A.: The vertical distribution of cloud feedback in coupled ocean-atmosphere models, *Geophys. Res. Lett.*, 38, L12704, doi:10.1029/2011gl047632, 2011.
- Stevens, B., Cotton, W. R., Feingold, G., and Moeng, C.-H.: Large-Eddy Simulations of Strongly Precipitating, Shallow, Stratocumulus-Topped Boundary Layers, *J. Atmos. Sci.*, 55, 3616–3638, doi:10.1175/1520-0469(1998)055<3616:lesosp>2.0.co;2, 1998.
- Stevens, D. E. and Bretherton, C. S.: Effects of resolution on the simulation of stratocumulus entrainment, *Q. J. Roy. Meteor. Soc.*, 125, 425–439, doi:10.1002/qj.49712555403, 1999.
- Twomey, S.: The Influence of Pollution on the Shortwave Albedo of Clouds, *J. Atmos. Sci.*, 34, 1149–1152, doi:10.1175/1520-0469(1977)034<1149:tiopot>2.0.co;2, 1977.
- Wielicki, B. A., Barkstrom, B. R., Harrison, E. F., Lee, R. B., Smith, G. L., and Cooper, J. E.: Clouds and the Earth's Radiant Energy System (CERES): An Earth Observing System Experiment, *B. Am. Meteorol. Soc.*, 77, 853–868, doi:10.1175/1520-0477(1996)077<0853:catere>2.0.co;2, 1996.
- Wilson, D.: The Large-Scale Cloud Scheme and Saturated Specific Humidity, UK Met Office Unified Model Documentation Paper 29, available at: [http://collab.metoffice.gov.uk/twiki/pub/Support/Umdp/029A\\_81.pdf](http://collab.metoffice.gov.uk/twiki/pub/Support/Umdp/029A_81.pdf) (last access: 14 April 2017), 2011.
- Wilson, D. R. and Ballard, S. P.: A microphysically based precipitation scheme for the UK meteorological office unified model, *Q. J. Roy. Meteor. Soc.*, 125, 1607–1636, doi:10.1002/qj.49712555707, 1999.
- Wood, R.: Drizzle in stratiform boundary layer clouds. Part 1: Vertical and horizontal structure, *J. Atmos. Sci.*, 62, 3011–3033, doi:10.1175/JAS3529.1, 2005.
- Wood, R.: Stratocumulus Clouds, *Mon. Weather Rev.*, 140, 2373–2423, doi:10.1175/MWR-D-11-00121.1, 2012.
- Wood, R. and Hartmann, D.: Spatial variability of liquid water path in marine low cloud: The importance of mesoscale cellular convection, *J. Climate*, 19, 1748–1764, doi:10.1175/JCLI3702.1, 2006.
- Wood, R., Bretherton, C. S., Leon, D., Clarke, A. D., Zuidema, P., Allen, G., and Coe, H.: An aircraft case study of the spatial transition from closed to open mesoscale cellular convection over the Southeast Pacific, *Atmos. Chem. Phys.*, 11, 2341–2370, doi:10.5194/acp-11-2341-2011, 2011a.
- Wood, R., Mechoso, C. R., Bretherton, C. S., Weller, R. A., Huebert, B., Straneo, F., Albrecht, B. A., Coe, H., Allen, G., Vaughan, G., Daum, P., Fairall, C., Chand, D., Gallardo Klenner, L., Garreaud, R., Grados, C., Covert, D. S., Bates, T. S., Krejci, R., Russell, L. M., de Szoeko, S., Brewer, A., Yuter, S. E., Springston, S. R., Chaigneau, A., Toniazzo, T., Minnis, P., Palikonda, R., Abel, S. J., Brown, W. O. J., Williams, S., Fochesatto, J., Brioude, J., and Bower, K. N.: The VAMOS Ocean-Cloud-Atmosphere-Land Study Regional Experiment (VOCALS-REx): goals, platforms, and field operations, *Atmos. Chem. Phys.*, 11, 627–654, doi:10.5194/acp-11-627-2011, 2011b.
- Xue, L., Chu, X., Rasmussen, R., Breed, D., Boe, B., and Geerts, B.: The Dispersion of Silver Iodide Particles from Ground-Based Generators over Complex Terrain. Part II: WRF Large-Eddy Simulations versus Observations, *J. Appl. Meteorol. Clim.*, 53, 1342–1361, doi:10.1175/jamc-d-13-0241.1, 2014.
- Xue, L., Chu, X., Rasmussen, R., Breed, D., and Geerts, B.: A Case Study of Radar Observations and WRF LES Simulations of the Impact of Ground-Based Glaciogenic Seeding on Orographic Clouds and Precipitation. Part II: AgI Dispersion and Seeding Signals Simulated by WRF, *J. Appl. Meteorol. Clim.*, 55, 445–464, doi:10.1175/jamc-d-15-0115.1, 2016.
- Yang, Q., W. I. Gustafson Jr., Fast, J. D., Wang, H., Easter, R. C., Morrison, H., Lee, Y.-N., Chapman, E. G., Spak, S. N., and Mena-Carrasco, M. A.: Assessing regional scale predictions of aerosols, marine stratocumulus, and their interactions during VOCALS-REx using WRF-Chem, *Atmos. Chem. Phys.*, 11, 11951–11975, doi:10.5194/acp-11-11951-2011, 2011.
- Zheng, X., Albrecht, B., Jonsson, H. H., Khelif, D., Feingold, G., Minnis, P., Ayers, K., Chuang, P., Donaher, S., Rossiter, D., Ghate, V., Ruiz-Plancarte, J., and Sun-Mack, S.: Observations of the boundary layer, cloud, and aerosol variability in the southeast Pacific near-coastal marine stratocumulus during VOCALS-REx, *Atmos. Chem. Phys.*, 11, 9943–9959, doi:10.5194/acp-11-9943-2011, 2011.
- Zuidema, P., Westwater, E., Fairall, C., and Hazen, D.: Ship-based liquid water path estimates in marine stratocumulus, *J. Geophys. Res.-Atmos.*, 110, D20206, doi:10.1029/2005JD005833, 2005.